Atmos. Chem. Phys., 12, 961–987, 2012
www.atmos-chem-phys.net/12/961/2012/
doi:10.5194/acp-12-961-2012

Atmospheric Chemistry and Physics

Distributions and regional budgets of aerosols and their precursors simulated with the EMAC chemistry-climate model

A. Pozzer[1,2,*], A. de Meij[1], K. J. Pringle[3], H. Tost[4], U. M. Doering[5], J. van Aardenne[6,], and J. Lelieveld[1,2,7]**

[1]The Cyprus Institute, Energy, Environment and Water Research Center, P.O. Box 27456, 1645 Nicosia, Cyprus
[2]Atmospheric Chemistry Department, Max-Planck Institute of Chemistry, P.O. Box 3060, 55020 Mainz, Germany
[3]School of Earth and Environment, Univ. of Leeds, Woodhouse Lane, Leeds, LS2 9JT, UK
[4]Institut für Physik der Atmosphere, Johannes-Gutenberg Universität Mainz, 55099, Mainz, Germany
[5]Federal Environment Agency (UBA), Wörlitzer Platz 1, 06844, Dessau, Germany
[6]European Commission Joint Research Centre, Institute for Environment and Sustainability, Ispra, Italy
[7]King Saud University, Riyadh 11451, Saudi Arabia
[*]now at: The Abdus Salam International center for Theoretical Physics, Earth System Physics section, Strada Costiera 11, 34151 Trieste, Italy
[**]now at: Air and climate change-mitigation, European Environment Agency, Kongens Nytorv 6, 1050 Copenhagen K, Denmark

Correspondence to: A. Pozzer (pozzer@cyi.ac.cy)

Received: 5 August 2011 – Published in Atmos. Chem. Phys. Discuss.: 9 September 2011
Revised: 2 December 2011 – Accepted: 29 December 2011 – Published: 19 January 2012

Abstract. The new global anthropogenic emission inventory (EDGAR-CIRCE) of gas and aerosol pollutants has been incorporated in the chemistry general circulation model EMAC (ECHAM5/MESSy Atmospheric Chemistry). A relatively high horizontal resolution simulation is performed for the years 2005–2008 to evaluate the capability of the model and the emissions to reproduce observed aerosol concentrations and aerosol optical depth (AOD) values. Model output is compared with observations from different measurement networks (CASTNET, EMEP and EANET) and AODs from remote sensing instruments (MODIS and MISR). A good spatial agreement of the distribution of sulfate and ammonium aerosol is found when compared to observations, while calculated nitrate aerosol concentrations show some discrepancies. The simulated temporal development of the inorganic aerosols is in line with measurements of sulfate and nitrate aerosol, while for ammonium aerosol some deviations from observations occur over the USA, due to the wrong temporal distribution of ammonia gas emissions. The calculated AODs agree well with the satellite observations in most regions, while negative biases are found for the equatorial area and in the dust outflow regions (i.e. Central Atlantic and Northern Indian Ocean), due to an underestimation of biomass burning and aeolian dust emissions, respectively. Aerosols and precursors budgets for five different regions (North America, Europe, East Asia, Central Africa and South America) are calculated. Over East-Asia most of the emitted aerosols (precursors) are also deposited within the region, while in North America and Europe transport plays a larger role. Further, it is shown that a simulation with monthly varying anthropogenic emissions typically improves the temporal correlation by 5–10 % compared to one with constant annual emissions.

1 Introduction

Tropospheric aerosols have significant effects on human health (e.g. Huntingford et al., 2007), the water cycle (e.g. Ramanathan et al., 2001) and climate (e.g. Isaksen et al., 2009). To study these different topics, global aerosol models that account for a wide range of complexities are required. Modelling work on aerosols chemistry (and their feedbacks) has been performed for over 30 yr (e.g. Atwater, 1975; Baklanov, 1988; Taylor and Penner, 1994), with the first global model to fully couple online meteorology-chemistry-aerosol-radiation on global scale (with inorganic partitioning) being developed by Jacobson (2000, 2001a,b) based on earlier work on a regional scale (Jacobson, 1997a,b), which included a large number of aerosol species. Nowadays, a number of global aerosol models that can treat semi-volatile inorganic species that partition between the gas and aerosol phases exist (e.g. Adams et al., 1999; Adams and Seinfeld, 2002; Bauer and Koch, 2005; Myhre et al., 2006; Feng and Penner, 2007; Pringle et al., 2010a), but most models treat five main aerosol species: black carbon (BC), particulate organic matter (POM), sulfate aerosol (SO_4^{2-}), mineral dust (DU) and sea spray (SS) (see Textor et al., 2006, and reference therein). Zhang (2008, and references therin) clearly describes the history of the chemistry models, showing the large increase in our understanding of the processes involved in aerosol formations and interactions.

Although models increasingly include sophisticated aerosol descriptions they still rely on offline calculated fields of aerosols and precursors emissions. The skill of the aerosol model strongly depends on the representativeness of the emission fields used, thus it is important to consider any possible biases in the emissions. For example, most of the global anthropogenic emissions inventories currently neglect the seasonal cycle of emissions for the majority of precursor gases and generally have a resolution of $1\times1°$ (e.g. van Aardenne et al., 2005; Olivier et al., 1999, 1996). Regional inventories of anthropogenic emissions are available at much higher resolution (both spatially and temporally) but they are spatially limited (e.g. Warneke et al., 2007; Jacobson, 2001c; Jacobson et al., 2007) and hence difficult (or impossible) to use in global models. The seasonal variation of anthropogenic emissions is important for many compounds (e.g. ammonia) especially for those for which the phase partitioning is temperature dependent (Pinder et al., 2004; De Meij et al., 2006). In this work, we take advantage of the state-of-the-art emissions inventory EDGAR-Climate Change and Impact Research (CIRCE), which provides emissions on a high spatial ($0.1\times0.1°$) and temporal (monthly) resolution, together with a recently developed aerosol scheme implemented within the EMAC model (Pringle et al., 2010a).

This study has three main objectives. The first objective is to evaluate the model performance in simulating aerosol and AODs calculations using the EDGAR-CIRCE emission inventory by comparing the results with ground based and space borne observations. The second objective is to analyse the aerosol (precursor) budget for five regions (Europe, North America, East Asia, South America and Central Africa) and quantify the aerosol import and export terms, compared with previous studies. Thirdly, we investigate the effect of including the seasonal cycle in the anthropogenic emissions of aerosol precursors, taking advantage of the newly developed emissions database. Therefore, a multi year model simulation with a relatively high horizontal resolution ($\sim1\times1°$) has been performed. Particular focus is placed on semi-volatile inorganic aerosol species (i.e. SO_4^{2-}, NO_3^- and NH_4^+) and their precursors.

The paper is organized as follows. Section 2.1 describes the model, the emission inventory and the observational datasets. In Sect. 3 the evaluation of the aerosol optical depth (AOD) is presented. AOD is a very useful metric for analyzing model performance in regions where ground-based observations are sparse. It provides an indication of the ability of the model to reproduce the concentrations of BC, OC and dust which are often not included in the observational networks. In Sect. 3.2 aerosol concentrations of SO_4^{2-}, NO_3^- and NH_4^+ are compared to large scale observations. Special focus is given to these compounds due to their complex interactions with the gas phase chemistry. Additionally, Na^+ aerosol is also compared to station observations as a proxy for sea salt. To examine the contribution of the different aerosol species to air quality, Sect. 4 shows the global and regional budgets of aerosol in North America, Europe, East Asia, Central Africa and South America. Finally, in Sect. 5 the effects of the seasonally varying anthropogenic emissions are analyzed, followed by the conclusions in Sect. 6

2 Model and observations

2.1 Model description and setup

EMAC is a combination of the general circulation model ECHAM5 (Roeckner et al., 2006) (version 5.3.01) and the Modular Earth Submodel System (MESSy, version 1.9, Jöckel et al., 2005). The model has been extensively described and evaluated (Jöckel et al., 2006; Pozzer et al., 2007), and additional details about the model system can be found at http://www.messy-interface.org.

In this study, the applied spectral resolution of the ECHAM5 base model is T106, corresponding to a horizontal resolution of the quadratic Gaussian grid of $\approx1.1\times1.1°$. The horizontal resolution has been chosen as a compromise between the resolution of the emissions inventories and computational resources. Emissions with different resolutions are available (ranging from $0.1\times0.1°$ to $1\times1°$, see Sect 2.1.1), but here the coarser resolution has been used in line with the model grid structure. Wild and Prather (2006), who performed a set of simulations at different resolutions (T21,T42, T63 and T106), showed that the simulated ozone is increasingly realistic (compared to the observations) with increasing resolution. In the literature not many studies at T106 resolution on a global scale are available; as an example, Lin et al. (2008) performed a simulation at this resolution, but it was limited to the summer of 1999, and not multi year as in this work. Higher resolutions are possible using the nesting techniques (Kerkweg and Jöckel, 2011; Hofmann et al., 2011), or by using a non-uniform (stretched) grid (Park et al., 2004a,b) to reduce the computational costs of the overall simulations. Nevertheless, it must be stressed that these techniques can be implemented only in few regions of interest. One of the main goals of this work is to take advantage of the relatively high resolution to study regional air pollution budgets (see Sect. 4) and thus it is essential to use a global model which provides consistent information within and between different regions.

The applied vertical resolution is 31 layers, up to 10 hPa. The model dynamics has been weakly nudged (Jeuken et al., 1996; Jöckel et al., 2006; Lelieveld et al., 2007) towards the analysis data of the European Centre for Medium-Range Weather Forecasts (ECMWF) operational model (up to 100 hPa) to represent the actual day-to-day meteorology in the troposphere. This allows a direct comparison with observations. The coupling between the radiation and the atmospheric composition has been removed (switched off). This implies that changes in the atmospheric composition calculated by the chemical mechanism (i.e. ozone, aerosols and greenhouse gases) do not induce a dynamical response of the model, which is instead forced by a climatological concentrations of such components. The model output is 5-hourly, thus an entire daily cycle is covered after 5 days. Dry deposition and sedimentation are described extensively in Kerkweg et al. (2006a) (DRYDEP and SEDI submodel) which are based on the big leaf approach. Dry deposition velocities depend on physical and chemical properties of the surface cover. Wet deposition is described in Tost et al. (2006a) (SCAV submodel), while its impact on atmospheric composition in the EMAC model is analyzed in detail in Tost et al. (2007a). The emission procedure has been explained by Kerkweg et al. (2006b) (OFFLEM, ONLEM and TNUDGE submodel) and Pozzer et al. (2006) (AIRSEA submodel). The chemistry is calculated with the MECCA submodel of Sander et al. (2005). The chemical mechanism is the one used in Jöckel et al. (2006, see electronic supplement), and consists of 104 gas phase species and 245 reactions. O_3 related chemistry of the troposphere is included, as well as non-methane-hydrocarbons (NMHCs) decomposition (von Kuhlmann at al., 2003). The other submodels used in this study are CONVECT (Tost et al., 2006b), LNOX (Tost et al., 2007b), as well as CLOUD, CVTRANS, JVAL, HETCHEM and TROPOP (Jöckel et al., 2006).

Aerosol microphysics and gas/aerosol partitioning are calculated by the Global Modal-aerosol eXtension (GMXe) aerosol module (described by Pringle et al., 2010a,b). GMXe simulates the distribution of sulfate, BC (Black Carbon), POM (Particulate Organic Matter), nitrate, ammonium, DU (Dust) and SS (Sea Spray) aerosol within 7 interacting lognormal modes (in a similar approach to that of Vignati et al., 2004; Stier et al., 2005; Mann et al., 2010). The particle number and mass of each mode is calculated prognostically but the geometric standard deviation is fixed (2.0 for the coarse modes hydrophobic, 2.2 for coarse mode hydrophilic, 1.59 for all other modes). The 7 lognormal modes span four size categories (nucleation (<5 nm radius), Aitken (5–50 nm), accumulation (50–500 nm) and coarse (>500 nm)) and are divided into a hydrophilic (4 modes) and a hydrophobic (3 modes) distribution. Hydrophobic aerosol (BC and DU) is emitted into the three modes in the hydrophobic distribution and hydrophilic aerosol (sulfate and sea spray) is emitted into the three largest modes of the 4-mode hydrophilic distribution. The emissions of POM are split between the hydrophobic (35 %) and hydrophilic (65 %) distributions. A parameterisation of aerosol ageing allows aerosol to pass from the hydrophobic to the hydrophilic distribution upon the addition of hydrophilic material (Vignati et al., 2004). The distribution of species within each mode is given in Pringle et al. (2010b, their Table 2). The aerosol within each mode is internally mixed while the 7 modes are externally mixed with respect to each other. Gas/aersosol partitioning is treated using the ISORROPIA-II model (Fountoukis and Nenes, 2007; Nenes et al., 1998a,b). In this study ISORROPIA-II is used to treat the interaction of NH_4, Na, SO_4, NO_3, Cl, H_2O aerosols. Gas-phase species considered are NH_3, HCl, HNO_3, H_2O. ISORROPIA-II solves for the equilibrium state by considering the chemical potential of the species (Nenes et al., 1998a,b). By considering specific compositional "regimes", it minimises the number of equations and iterations required. In this study activity coefficients are taken from pre-calculated lookup tables to reduce computational expense (see also Pringle et al., 2010b).

The optical properties of the aerosol are calculated with the EMAC submodel AEROPT. It is based on the scheme by Lauer et al. (2007) and makes use of predefined lognormal modes (i.e. the mode width σ and the mode mean radius have to be taken into account), for which lookup tables with the extinction coefficient $\sigma_{\rm sw}$, the single scattering albedo $\omega_{\rm sw}$ and the assymetry factor $\gamma_{\rm sw}$ for the shortwave and extinction coefficient $\sigma_{\rm lw}$ for the longwave spectrum have to be created.

These lookup tables are calculated with the help of the LIBRADTRAN (Mayer and Kylling, 2005) for various aerosol types. In the case of the AEROPT submodel the considered species are POM, BC, DU, SS, water soluble compounds (WASO, i.e. all other water soluble inorganic ions, e.g.: NH_4^+, SO_4^{2-}, HSO_4^-, NO_3^-, etc.) and aerosol water (H_2O). The refractive indices for these compounds are taken from several data bases, e.g. HITRAN2004 :

- WASO (mainly using ammonium sulfate values following Hess et al., 1998),
- BC (Hess et al., 1998),
- SS (Shettle, 1979),
- H_2O (Hale and Querry, 1973),
- OC (Hess et al., 1998; Sutherland and Khanna, 1991; S. Kinne, personal communication, 2010),
- DU (Hess et al., 1998; S. Kinne, personal communication, 2010).

For these compounds the wavelength dependent complex refractive index is used for a comprehensive set of Mie calculations. This results in a 3-dimensional lookup table (depending on the complex refractive index and the Mie size parameter, combining the wavelength and aerosol size information) spanning up a $100 \times 100 \times 100$ space.

During the simulation, the volume-weighted mean complex refractive index is determined for each mode of the aerosol distribution. Then, depending on the mean radius of the mode, the Mie size parameter is calculated for each wavelength band. These three parameters provide the required information for the lookup table for the values for σ_{sw}, ω_{sw}, γ_{sw} and σ_{lw}. To cover the wavelength dependency these coefficients are determined for 16 predefined bands in the shortwave and 16 in the longwave spectrum, which are not required to match the bands used in the radiation calculation of the base model (in our case ECHAM5). Next a mapping of the precalculated wavelength bands to those of the radiation scheme is performed using a weighted interpolation, using a (constant) reference spectrum for the solar incoming flux at the Earth surface in which trace gas absorption based on climatological values has been considered. This method is also applied to determine the values for other (diagnostic) wavelengths, e.g. for the 550 nm band, which is often used in observational data sets. Finally, the method of calculating the AOD is the following: for each mode the extinction coefficient is calculated for a single particle; the extinction coefficient is then multiplied by the number of particles per grid cell, giving the vertical integral of the extinction per mode and per layer. The AOD per layer is obtained by adding all the modes in the layer, and the sum of all AOD values over the vertical model domain yields the total atmospheric AOD.

The model simulation covers the years 2004–2008. The first year is used as spin-up for the model and only the years 2005–2008 are used in this study. These years are expected to be represented by the model with high consistency, because the chosen emission setup of primarily emitted species was compiled for the year 2005 (see below).

2.1.1 Emissions

The high resolution global anthropogenic emission inventory (1990–2005) EDGAR-CIRCE (Doering et al., 2009a,c) which was used in this study has been prepared in the framework of the CIRCE (Climate Change and Impact Research: the Mediterranean Environment) Project by the EDGAR (Emission Database for Global Atmospheric Research) group of the EC-Joint Research Center Ispra (Italy), Climate Change Unit. This dataset includes greenhouse gases, NO_x, CO, Non-Methane Volatile Organic Compounds (NMVOCs), NH_3 and SO_2 from fossil fuel and biofuel related emissions. Emissions from international aviation were calculated for the period 1990–2005 using a technology based emission factor approach (Eyers et al., 2004). International shipping emissions are based on the QUANTIFY project (Hoor et al., 2009). The EDGAR-CIRCE data has been compared to other emissions inventories by Doering et al. (2009b). This comparisons reveals that the EDGAR-CIRCE emissions are in line with other global (Bond et al., 2007; UNF, 2008) and regional (Ohara et al., 2007; Streets et al., 2003; Klimont et al., 2002; Vestreng and Klein, 2002) data sets and the differences lie within the uncertainties associated with emissions estimates. In particular, over Europe, the EDGAR-CIRCE emissions inventory are significantly higher than the regional anthropogenic emissions inventory EMEP (Vestreng et al., 2007, 2009). As an example SO_2 emissions from EDGAR-CIRCE are ∼80 % higher compared to the EMEP inventory (9.9 and 5.5 Tg S yr^{-1}, respectively), while smaller differences are present for NO_x (4.7 and 3.9 Tg N yr^{-1}, respectively) and NH_3 (5.3 and 3.5 Tg N yr^{-1}, respectively). Nevertheless the total European SO_x, NO_y and NH_3 emissions in the EDGAR-CIRCE inventory (11.2 Tg S yr^{-1}, 5.1 and 5.3 Tg N yr^{-1}, respectively) are in line with the work of Aan de Brugh et al. (2011) (11.4 Tg S yr^{-1}, 7.2 and 6 Tg N yr^{-1}, respectively), who used different anthropogenic emissions (Dentener et al., 2006). The EDGAR-CIRCE anthropogenic emissions over Asia are quite different from those estimated by the REAS (Regional Emission inventory in ASia) database (Ohara et al., 2007) for the year 2005, although the differences are well within the errors associated with the emissions estimates of the region. The anthropogenic emissions from the EDGAR-CIRCE inventory are within 20 % of the REAS database for BC (∼1.4 and 1.3 Tg yr^{-1}, respectively) and NO_x (∼6.8 and ∼6.0 Tg N yr^{-1}, respectively), but quite different values are found for NH_3 (∼6.1 and ∼10.4 Tg N yr^{-1}, respectively), SO_2 (∼24.0 and ∼18.2 Tg S yr^{-1}, respectively) POM (∼5.5 and ∼3.9 Tg yr^{-1}, respectively). Nevertheless the values used in this work are in line with other literature estimates for these compounds (Streets et al., 2003; Streets and Waldhoff, 2000). This emphasizes the difficulties of constraining the emissions, especially in this region.

The anthropogenic emissions were distributed vertically as described in Pozzer et al. (2009), and the chosen vertical distribution of the emissions is based on the EMEP (European Monitoring and Evaluation Programme) model (Dimitroulopoulou and ApSimon, 1999; Simpson et al., 2003), applied after the analysis of stack plume data from Eastern Europe. As shown in Pozzer et al. (2009) and De Meij et al. (2006), the injection height of the emissions is very important in global and regional models, leading to an improvement of up to 30 % in the correlation with station observations compared to simulations where the emissions are not vertically distributed (i.e. released from the surface). The EDGAR-CIRCE emissions dataset has a spatial resolution of $0.1 \times 0.1°$. The standard temporal resolution is annual, and only the data for year 2005 has been produced with higher resolution (monthly). Hence, in this study, only the emissions for the year 2005 have been used to take advantage of high temporal and spatial resolution. The biogenic emissions of organic species have been represented following Guenther et al. (1995) and are computed offline in the model (Ganzeveld et al., 2006) with monthly temporal resolution. The natural emissions of NH_3 are based on the GEIA

Table 1. Global gas emissions for the year 2005 in $Tg\,yr^{-1}$. In bold are the emissions calculated on-line by the submodels ONLEM or AIRSEA (maximum and minimum) during the 2005-2008 period.

Trace gas	Anthropogenic[a]	Biomass burning[b]	Natural	Total
CO	584.1	356.8	112.4	1053.3
C_2H_4	6.9	3.6	11.3	21.8
C_2H_6	7.5	2.0	0.5	10.1
C_3H_6	3.0	1.6	3.4	8.0
C_3H_8	9.0	0.6	0.3	10.0
C_4H_{10}[c]	63.0	0.8	0.4	64.2
MEK[d]	7.0	3.1	–	8.2
CH_3CHO	1.5	1.4	–	2.9
CH_3COCH_3	4.1	1.3	55.6	61.0
CH_3COOH	4.8	4.6	3.4	12.7
CH_3OH	7.6	4.6	150.1	162.3
HCHO	3.4	2.4	–	5.9
HCOOH	2.6	2.5	5.6	10.7
SO_2	140.4	2.3	29.1	171.9
NH_3	40.7	–	10.6	51.3
DMS	–	–	**44.6–45.6**	45.3
ISOPRENE	–	–	**394.9–420.8**	408.0
NO_x[e]	27.9	4.6	**7.7–8.6**	41.0

[a] Based on the EDGAR-CIRCE inventory for the year 2005.
[b] From GFEDv3.1 (van der Werf et al., 2010), averaged over the years 1997–2009.
[c] It includes higher alkanes.
[d] Methylethylketone plus all higher ketones.
[e] In units of $Tg\,N\,yr^{-1}$. The natural emissions include soil and lightning sources.

database (Bouwman et al., 1997). Both these datasets have a $1 \times 1°$ horizontal resolution. NO_x produced by lighting is calculated online and distributed on different vertical levels, based on the parametrization of Price and Rind (1992). The emission of NO from soils is calculated online based on the algorithm developed by Yienger and Levy (1995) and depends on ecosystem type, soil moisture state and the surface temperature. The underlying ecosystem map was compiled by Olson (1992) and is also used to estimate the isoprene emissions with the ONLEM submodel. Volcanic emissions of SO_2 are based on the AEROCOM data set (Dentener et al., 2006), with background emissions from continuous and explosive volcanoes. The biomass burning contribution was added using the Global Fire Emissions Database (GFED version 3, van der Werf et al., 2010) covering the years 1997–2009 with a $0.5 \times 0.5°$ spatial resolution and a monthly temporal resolution. The fuel burnt areas used in the GFED database is based on the work of Giglio et al. (2010), estimated from four satellite datasets. The AIRSEA submodel (Pozzer et al., 2006) calculates the oceanic DMS emissions online, with prescribed sea water DMS concentrations from Kettle et al. (1999). Additionally AIRSEA calculates isoprene emissions, where the water isoprene concentration was estimated from chlorophyll concentrations (Conkright et al., 2002) based on the work of Broadgate et al. (2000). Finally, AIRSEA estimates the methanol (CH_3OH) water deposition, based on an undersaturation of the oceanic surface water of 0.94. The atmosphere-ocean transfer velocity parametrization is based on Wanninkhof (1992). The total gas-phase emissions are shown in Table 1.

Table 2. Global aerosol emissions for the year 2005 in $Tg\,yr^{-1}$.

Aerosol	Anthropogenic[a]	Biomass burning[b]	Natural[c]	Total
BC	6.0	2.1	–	8.1
POM	18.8	25.8	19.1	63.7
DU	–	–	1670	1670
SS	–	–	7890	7890

[a] From based on the EDGAR-CIRCE inventory, for the year 2005.
[b] From GFEDv3.1 (van der Werf et al., 2010), averaged over the year 1997–2009.
[c] From AEROCOM (Dentener et al., 2006).

Anthropogenic bulk aerosol emissions are also based on the EDGAR-CIRCE emissions inventory. Biomass burning BC and POM are based on the GFEDv3.1 emission database. Secondary Organic Aerosol (SOA) particles are directly emitted as POM, assuming that 15 % of natural terpene emissions form SOA (Guenther et al., 1995). Emission of dust and sea spray aerosol are treated using offline monthly emission files based on AEROCOM. Offline emission of dust and sea spray have been used in this study because of their extensive use and evaluation in a number of studies, and to increase the comparability with the work of Pringle et al. (2010a).

2.2 Satellite observations

2.2.1 MISR

The Multi-angle Imaging SpectroRadiometer (Diner et al., 1998, MISR) instrument flies on the Terra satellite and has been operational since February 2000. The instrument is designed to measure the solar radiation reflected by the Earth system by a multiple camera configuration (four forward, one nadir and four backward). Each camera measures in four different wavelengths centred at 446 nm (blue), 558 nm (green), 671 nm (red) and 866 nm (near-infrared). In this study Level 3 Component Global Aerosol Product version F15 (CGAS-F15) are used, specifically the AOD (Average Optical Depth), which is derived from Level 1 and Level 2 products, averaged over a month and stored on a geographic grid of $0.5 \times 0.5°$. This observational dataset present monthly resolution. A comparison over land and ocean with AERONET (AErosol RObotic NETwork) data has shown that MISR AODs are within 0.05–20 % of that of AERONET (Kahn et al., 2005, 2010). MISR AODs can be obtained from https://wist.echo.nasa.gov/api/.

2.2.2 MODIS

The MODerate resolution Imaging Spectro-radiometer (MODIS) instrument also flies on the Terra satellite. In contrast to MISR, the MODIS instrument has only one camera which measures radiances in 36 spectral bands. Daily Level 2 (MOD04) aerosol optical depth products (550 nm) are produced on a spatial resolution of 10×10 km over land, using the 1×1 km cloud-free pixel size. The MODIS Level 2 product refers to a swath width of about 2330 km, therefore the instrument has almost daily global coverage. In this study global Level 3 AOD (version MOD08) Collection 005 products are used (field `Optical_Depth_Land_And_Ocean_Mean`). The level 3 AOD product is derived from the statistics of the Level 2 products and stored on a $1 \times 1°$ grid with a monthly temporal resolution in the MOD08 Level 3 product file. Reported MODIS AOD uncertainties are $\pm 0.05 \pm 0.15 \times$ AOD (Remer et al., 2008; Levy et al., 2010). Although MODIS aerosol products are provided over land (Kaufman et al., 1997) and water surfaces (Tanré et al., 1997), it is important to underline that no aerosol retrieval is possible over bright surfaces such as deserts and ice. MODIS AODs can be obtained from https://wist.echo.nasa.gov/api/.

2.3 In situ observations

2.3.1 CASTNET

The Clean Air Status and Trends Network (CASTNet) comprises 86 sites located in or near rural areas of the United States, administered and operated by the Clean Air Markets Division (CAMD) of the United States Environmental Protection Agency (EPA) (Edgerton et al., 1990). CASTNET is the USA's primary monitoring network for measuring concentrations of air pollutants. All sites utilize Teflon filters to collect particulate sulfate (SO_4^{2-}), nitrate (NO_3^-), and ammonium (NH_4^+). The sampling is conducted on a weekly basis. The usage of Teflon filters in the network for nitrate particle collection is known to underestimate the effective concentration of NO_3^- (Ames and Malm, 2001), due to temperature-dependent volatilization (Hering and Cass, 1999), or by reaction with strong acids under ammonia limited conditions (Appel et al., 1988). In this work we only use data from stations with continuous coverage for the years 2005–2008 (33 stations in total). The data were downloaded from http://www.epa.gov/castnet.

2.3.2 EMEP

The European Monitoring and Evaluation Programme (EMEP Hjellbrekke and Fjæraa, 2011) is a scientifically based and policy driven programme under the Convention on Long-range Transboundary Air Pollution for international co-operation to help solving transboundary air pollution problems. Parties to the Convention on Long-Range Transboundary Air Pollution perform monitoring at regional monitoring sites across Europe. The data are subject to national quality assessment prior to submission to the EMEP Chemical Coordinating Centre at NILU (Norwegian Institute for Air Research). The number of stations used in the comparison ranges from 59 (for SO_4^{2-}) to 31 (for NO_3^- and NH_4^+). Due to the partial usage of Teflon filters (depending on the station/country), observations from this network are also expected to underestimate NO_3^- concentrations. The data were downloaded from http://www.nilu.no/projects/ccc/emepdata.html.

2.3.3 EANET

The Acid Deposition Monitoring Network in East Asia (EANET) was established as an initiative for regional cooperation among the participating countries, creation of a common understanding of the state of acid deposition problems and for providing useful inputs to policy makers at various levels. Regular monitoring activities started in January 2001 with the participation of 10 countries, namely China, Indonesia, Japan, Malaysia, Mongolia, Philippines, Republic of Korea, Russia, Thailand, and Viet Nam. Cambodia, with Lao People's Democratic Republic and Myanmar joining EANET in 2001, 2002 and 2005, respectively. Acid deposition monitoring of EANET addresses four environmental issues: wet deposition, dry deposition (air concentration), soil and vegetation, and inland aquatic environment. In this work, data from 28 stations of the EANET network are used. The data were downloaded from http://www.eanet.cc/product/index.html (Asia Center for Air Pollution Research (ACAP), 2011).

3 Comparison with observations

In the following sections, a comparison of the model results with observations is performed. All the observational data have been collected at (or reduced to) monthly averages. Firstly, the global AOD will be analyzed to obtain an overall picture of the model performance on a large scale. This comparison is important for regions where no direct information about concentrations are available. The explicit AOD calculation during the simulation allows a more detailed analysis than that performed by Pringle et al. (2010a), who used an offline simplified treatment of AOD based on the parametrization of Kiehl and Briegleb (1993).

After the evaluation of AOD, the simulated aerosol mass concentrations are compared to measurements taken from observational networks in North America, Europe and Asia.

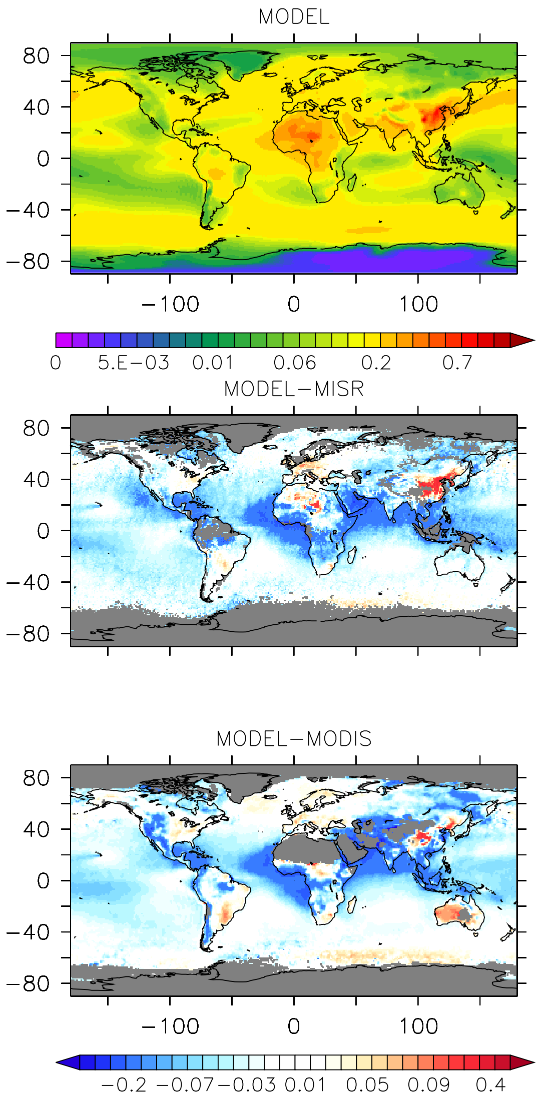

Fig. 1. Top: annual average AOD modelled by EMAC for the years 2005–2008. Bottom: annual average AOD difference between model results and MODIS and MISR observations (level 3 product) for the years 2005–2008. In grey the regions with less than 12 observations during the period considered.

3.1 Comparison with satellite observations

In Fig. 1 the 2005–2008 average AOD simulated by EMAC is shown, together the differences between these values and the 2005–2008 averaged satellite observations. In general, the AOD simulated by the model corresponds well with the observations for large areas of the globe (with a relative difference below 30 %). Compared to MODIS AOD observations, the model appears to be generally low-biased (in terms of relative difference) by 70 % over the Southern Pacific Ocean, Northwestern America and North East Asia, while compared to MISR this bias is much smaller (∼40 %). Highest relative overestimations appear over South America and South Africa (80 %) for modelled AOD compared to MODIS observations, while the maximum overestimation is ∼50 % over East Asia when compared to MISR observations. A strong underestimation of the model with respect to the observed AODs (both for MODIS and MISR observations) is found over some tropical oceans, especially over the Central Atlantic ocean, the Northern Indian Ocean, the Malaysian region and over the Gulf of Mexico (∼50 % or ∼0.2) for both observational datasets. The underestimation could be related to the uncertainties (underestimation) in the emissions for dust and biomass burning in the inventory or overestimation of the deposition over marine regions. However, some underestimation of the emissions is most probable. Dust, in fact, is only emitted at the lowest level of the model, hence neglecting the strong dust plume episodes which can uplift and transport dust over larger distances. This is confirmed by a good spatial correlation of AOD between satellite and model results during the winter season, when the dust storm episodes are reduced in number with respect to the summer season (see below). Additionally, the biomass burning emissions of BC and POM in the inventory (2.12 and 18.45 $\mathrm{Tg\,yr^{-1}}$, respectively) may be underestimated, as they are lower than what is suggested in the literature (3.1 and 34.7 $\mathrm{Tg\,yr^{-1}}$, respectively, Dentener et al., 2006). The underestimations of the biomass burning sources has been noticed for the same simulation also for other emitted compounds (CO, Liu et al., 2011) when compared to satellite observations. The underestimation could possibly produce a bias in the AOD estimates by the model, which results in an underestimation of AOD when compared with MODIS and MISR, as observed e.g. over the Central Atlantic Ocean. The underestimation of AOD over the Northern Indian Ocean is consistent with an underestimation of the dust outflow from the Arabian peninsula, while the underestimation of the AODs over the Indian subcontinent indicates too low emissions of anthropogenic/biomass burning origin. The largest effect of the underestimation of the biomass burning emissions can be found over the Malaysian region, where the simulated AOD is consistently underestimated (∼0.2) with respect to the MODIS and MISR observations. Over China (more specifically inland) the model tends to overestimate the AODs. The cause is not clear, as the next sections indicate that the model does not overestimate anthropogenic aerosol compounds in this region. We speculate that this might be related to the definition of aerosol versus thin cloud in the satellite retrieval algorithm, because in this region high level of pollution are often associated with "haze clouds", which might be rejected as cloud contamination (Ma et al., 2010).

Further, the model shows discrepancies with the MODIS observations also over the western part of the USA and Canada. In fact, although good agreement is also found over Europe and Northeastern America (below 30 % difference both for MODIS and MISR), for West USA the satellite AOD observations are lower than the modelled ones (70 and 30 % for MODIS and MISR, respectively). Generally, the

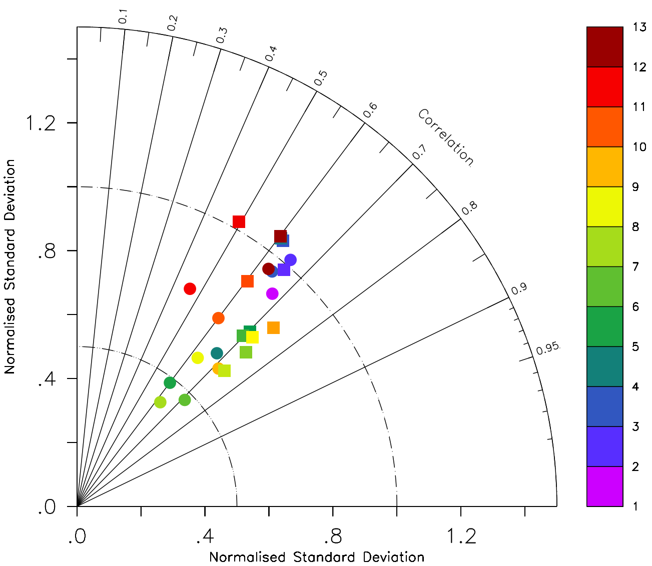

Fig. 2. Taylor diagram of the comparisons between satellite observations and model results of AOD. The comparison with MODIS and MISR are depicted with squares and circles, respectively. The color code denotes the month of the year.

model tends to agree better with MISR than MODIS observations. The MISR instrument registers AODs over bright surfaces, which allows us to evaluate calculated AODs e.g. over the Arabian peninsula. Over this region the model underestimates the observed AODs, most probably due to an underestimation of the dust emissions. Note that a new dust emission routine is under development for the EMAC model, to improve this aspect in the near future.

To further quantify the ability of the model to reproduce the spatial distribution of the AODs observed by MODIS and MISR, in Fig. 2 we present a Taylor diagram of the comparison on a monthly basis. It shows the correlation coefficient between model results and observations (R) by the angle to the ordinate. The standard deviation of the model normalised to the standard deviation of the observations ($\sigma_{\mathrm{model}}/\sigma_{\mathrm{obs}}$) is represented by the distance from the origin. The standard deviation was estimated using the root mean square difference (in space) from the spatial average, each estimated from the set of multi year monthly values. The standard deviation represents the spatial variability of the data from each set of temporal means (month). The observations (i.e. MODIS or MISR) are therefore located at a correlation of 1 and a normalised standard deviation of 1. The distance between a point and this "ideal" point is the centered pattern root mean square. The better a model reproduces the observations, the closer the resulting points are located to this "ideal" point. A detailed explanation of this type of diagram has been presented by Taylor (2001). While the spatial correlation between model results and observations is generally good (higher than 0.5), the normalised standard deviation is mostly below one, indicating that strong spatial gradients between regions of high AODs and low AODs are not well reproduced.

The model reproduces the satellite observations with a high degree of consistency during winter time. It is clear from Fig. 2 that despite the relatively high correlation (0.6–0.7), for spring and summer months (April until September) we obtain a normalised standard deviation of the model compared to the observations of ~0.6 (MODIS) and ~0.4 (MISR). In autumn and winter the model simulates the AOD with a higher level of agreement. Not only are the spatial correlation coefficients around 0.5–0.6, but the normalised standard deviation is close to unity, especially during January–March.

After the analysis of the spatial distribution for different months, the ability of the model to reproduce the seasonal cycle of the observed AODs is also investigated. The temporal correlation coefficients between the observations and model results are shown in Fig. 3. This has been calculated based on monthly values of the observational dataset and monthly averages of the model results for the period 2005–2008. It indicates whether the model is able to reproduce the observed seasonal cycle (if present), independent of biases between observations and model results. A low correlation (close to zero) implies either a wrong representation of the seasonal cycle by the model or the lack of a well defined seasonal cycle in the model and/or observations. The temporal correlation is, with respect to the MODIS and MISR observations, low over some oceanic regions (i.e. Southern Indian Ocean and Southern Pacific Ocean) due to the low seasonal variation in the emissions of sea salt. Outside Europe and the USA the information about the seasonal variation is often not available, which is one of the reasons that these variations are normally not included in global emission inventories of anthropogenic emissions (De Meij et al., 2006). Although the modelled AODs are generally lower than the observed AODs over Central Africa, the seasonality of the AOD represents the observations, with temporal correlation coefficients higher than 0.7. High temporal correlation coefficients (0.8) are also found over Malaysia, which indicates that the model is correct in timing the biomass burning emissions for this region. Very good correlation (higher than ~0.7) with both observational datasets is found for the Arabian region. This indicates that the timing of dust events in the regions (i.e. the transport) is correctly reproduced, at least partially related to the nudging of the meteorology (and thus of transport). Nevertheless, as mentioned earlier, the calculated AODs are lower compared to the observed AODs, due to the constant emissions of dust in the model, which are prescribed offline. A good correlation (~0.6–0.8) is obtained over North Africa, the Central Atlantic Ocean and the Southern Europe when compared to MISR observations. This indicates that the dust intrusions over these regions are correctly timed by the model, although (as noted before) their intensity is generally underestimated. It must however be

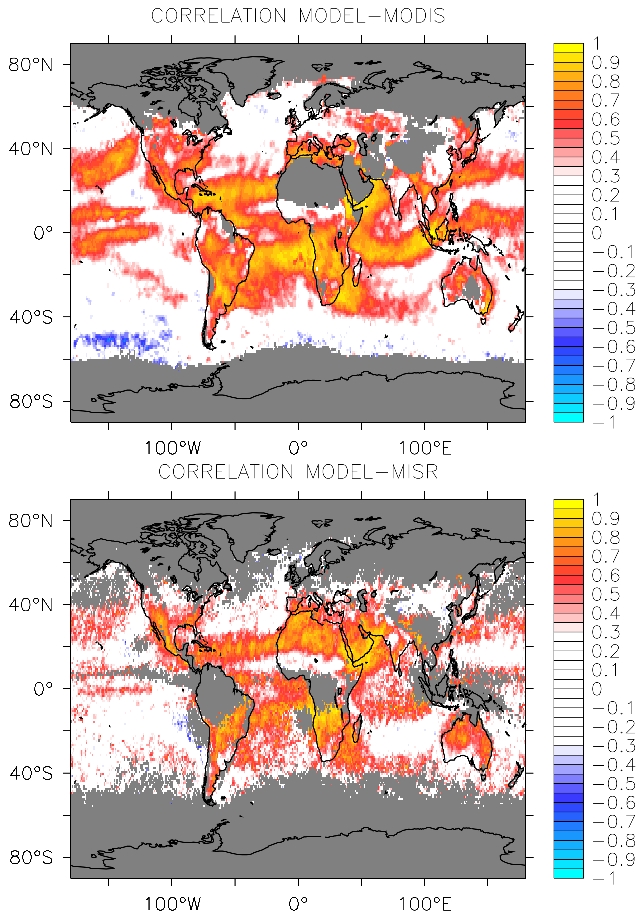

Fig. 3. Correlation (R) between model results and MODIS and MISR observations (level 3 product) of AOD. In grey the regions with less than 24 observations/months present during the years 2005–2008.

underlined, that the modelled AOD in the dust outflow regions is strongly affected by the conversion rate from hydrophobic to hydrophilic via condensation and coagulation with hydrophilic material, which affects the removal by deposition processes, and that this effect may play a role in the underestimation of AOD in these regions.

3.2 Station observations

To evaluate the calculated global concentrations of aerosol sulfate, nitrate and ammonium, the multiyear model results (2005–2008) are compared with measurements from different monitoring networks. We selected the stations for which data is available for the complete time period (i.e. between 2005–2008). The model has been sampled in the same location as the observations in order to have co-located model results and observations. In Fig. 4 some examples of the temporal development of the model results and observations are shown for the different locations and aerosol species.

In the following sections (Sects. 3.2.1–3.2.4), a standard set of figures is presented (Figs. 5–12). The maps in Figs. 5, 7, 9 and 11 present at the top the multi year annual average of the model with the multi year annual average of the observations overplotted (both in µg m^{-3}) and at the bottom the correlation coefficients between model results and observations, based on the monthly values. In Figs. 6, 8 and 10 on the left side the scatter plots of all the available data (monthly values) are presented, while on the right side the Taylor diagrams are shown. In these diagrams the data are grouped per month, and all data available for a certain month (independent of the year) are used in the calculation. The Taylor diagrams, therefore, give information about the spatial correlations (and normalised standard deviation) between observations and model results for each month. For Na^+, only the scatter plots are shown (Fig. 12). In Table 3, an overview of the comparison between the model results and the observations is presented, as discussed in the following sections.

3.2.1 SO_4^{2-}

Overall the model accurately reproduces the observed concentrations of SO_4^{2-}, with more than 88, 92 and 95 % of the model results within a factor of two of the observations based on the EANET, EMEP and CASTNET networks, respectively (see Table 3). In general the Root Mean Square error (RMS) is well below the observational standard deviation, which is one of the conditions for good quality modelling results (Barna and Lamb, 2000). The yearly average concentrations are reasonably well captured (see Fig. 5), indicating that the spatial gradients of the monthly mean concentrations are sufficiently well reproduced by the model. The model calculates high sulfate concentrations over Europe and East USA (up to 9 and 7 µg m^{-3}, respectively) and very high concentrations over East China and other parts of East Asia (up to 25 µg m^{-3}). The East-West gradient in the USA and the South-North gradient in Europe are reproduced (although it is less distinct over the USA, see below), while the gradients over East Asia are underestimated. It must however be stressed that the number of stations used in the comparison not only is the lowest for the EANET network (26 stations), but also that this network covers a much larger region than the CASTNET and EMEP networks. The spatial gradients (i.e. the Taylor diagram) could therefore be strongly influenced by the station distribution, and the representativeness of the comparison is limited.

Figure 6 shows the comparison between the simulated SO_4^{2-} and the different observations network. The general underestimation of SO_4^{2-} by the model (see the Model Arithmetic Mean (MAM) and the Observations Arithmetic Mean (OAM) in Table 3) is clear from the comparison with the CASTNET and EANET datasets (see also Figs. 4 and 6, scatter plot) and partially from the comparison with the EMEP dataset. Also the simulated spatial variability is lower than observed, as noticeable in the Taylor diagrams where the

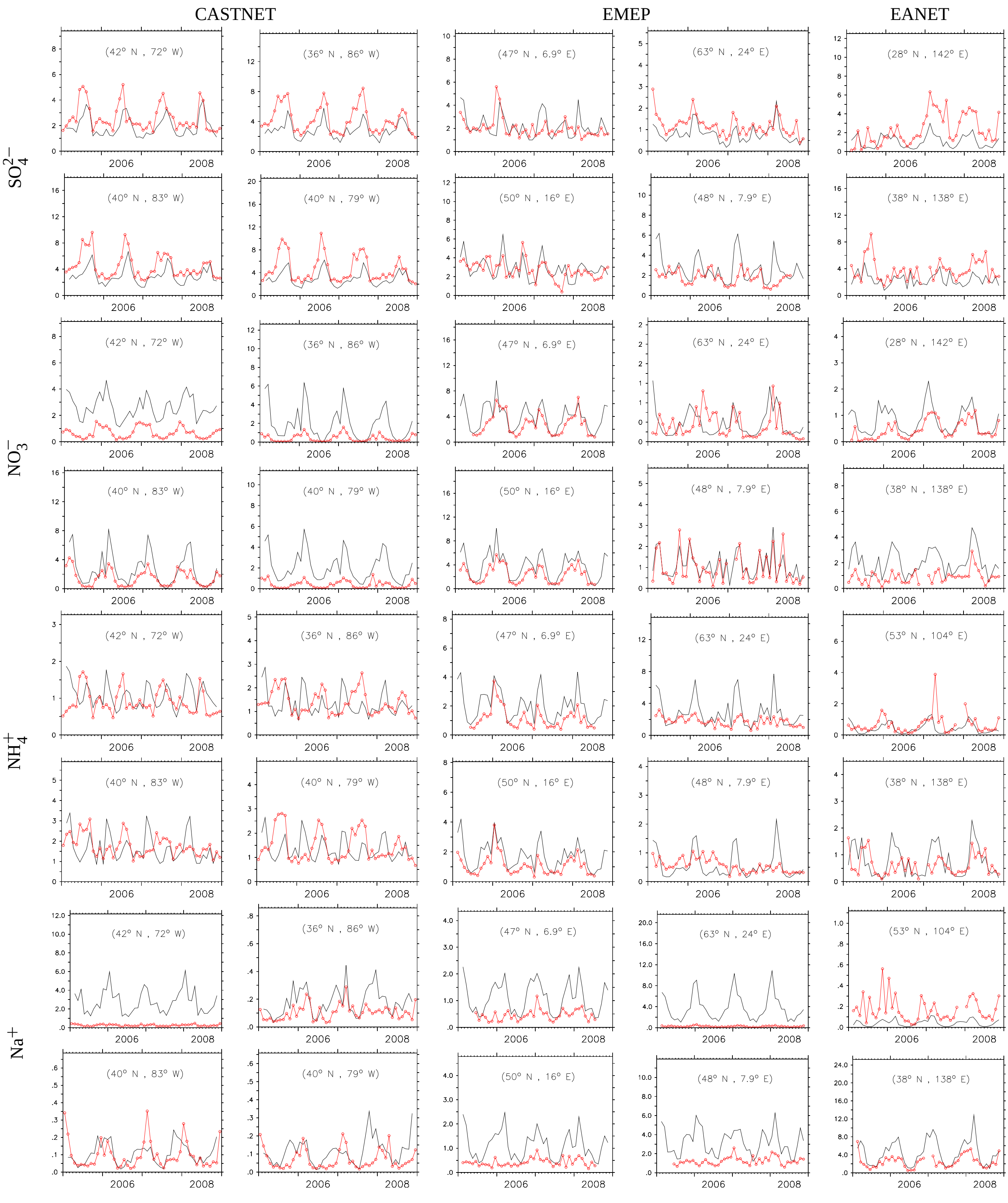

Fig. 4. Comparison of simulated and observed SO_4^{2-}, NO_3^-, NH_4^+ and Na^+ concentrations (in $\mu g\,m^{-3}$) for some selected locations. The red lines represent the observations, while the simulated monthly averages are indicated by the black lines. The location of the stations (longitude and latitude) is at the center of each plot. Note the different scales of the vertical axes.

Table 3. Summary of the comparison of model results to observations of aerosol concentrations. OAM and MAM are the arithmetic mean of the observations and of the model, respectively (in $\mu g\,m^{-3}$), while OSTD and MSTD are the standard deviation of the observations and of the model, respectively (in $\mu g\,m^{-3}$). MAM and MSTD were calculated by sampling the model at the locations of the observations and monthly averaged as the observations, over the 2005–2008 period. MAM, OAM, MSTD and OSTD represent co-located measurements and model results. PF2 is the percentage of modelled point within a factor of two of the observations. RMS denotes the Root Mean Square error.

Species	Network	n. stations	MAM	MSTD	OAM	OSTD	MAM/OAM	PF2	RMS
SO_4^{2-}	CASTNET	32	2.1	1.2	2.9	2.0	0.7	95.3	1.2
SO_4^{2-}	EMEP	58	1.6	1.1	1.9	1.3	0.8	92.3	1.2
SO_4^{2-}	EANET	26	2.4	1.9	4.4	5.3	0.5	88.7	4.7
NO_3^-	CASTNET	32	1.7	1.7	0.9	1.1	1.9	46.0	1.2
NO_3^-	EMEP	30	2.5	2.2	1.6	2.0	1.6	64.5	2.1
NO_3^-	EANET	26	1.9	2.2	1.2	2.2	1.6	52.0	2.6
NH_4^+	CASTNET	32	1.0	0.7	1.0	0.7	1.0	87.7	0.6
NH_4^+	EMEP	30	1.2	1.2	0.9	0.8	1.3	80.6	0.8
NH_4^+	EANET	26	0.9	1.1	1.1	1.6	0.8	81.9	1.5
Na^+	CASTNET	32	0.3	0.6	0.1	0.1	3.2	49.8	0.5
Na^+	EMEP	23	3.5	3.5	0.9	1.8	3.9	15.7	3.2
Na^+	EANET	26	2.9	2.9	1.0	1.6	2.8	33.8	2.6

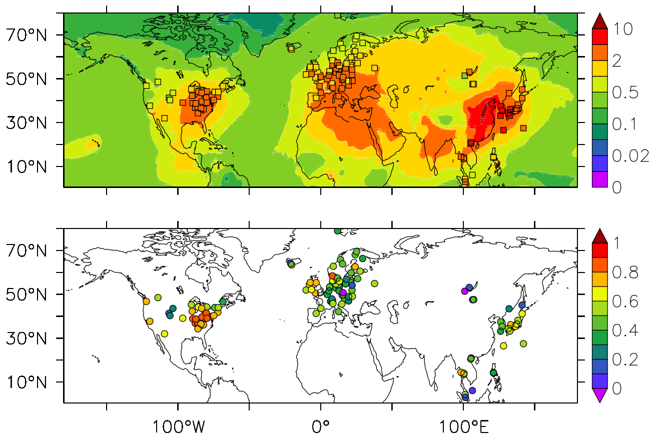

Fig. 5. UPPER: simulated mean concentrations of SO_4^{2-} (in $\mu g\,m^{-3}$) for the year 2005–2008, with observations from CASTNET, EMEP and EANET (averaged over the same period) overplotted. LOWER: temporal correlation of observations from CASTNET, EMEP and EANET and model results for SO_4^{2-}.

normalised standard deviation is generally ∼0.5 for comparison with CASTNET and EANET, while with EMEP it is between ∼0.5 and ∼1. Notably, the lowest values of normalised standard deviations appear during winter months (November–January). During the summer months (June and July) the normalised standard deviations are close to the ideal value of 1. The simulation results agree very well with the CASTNET network observations, where a spatial correlation higher than ∼0.7 (Fig. 5, top) is achieved, with peaks of 0.95 during the Summer and Autumn. This implies that the observed spatial distribution is accurately reproduced by the model, although the gradients are less pronounced than observed. The comparison with the EMEP network observations again shows the lowest value of the spatial correlation during the winter season.

The general underestimation of the model results compared to the CASTNET observations does not seem to influence the overall agreement of the seasonal cycle of SO_4^{2-}, which is very well reproduced in the USA (see Fig. 5, lower panel). In the USA the model reproduces (with a temporal correlation value above 0.7 in most locations) the observed seasonality, with the unique exception of stations located in the Central USA. Compared to EMEP and EANET, however, the model results have a somewhat lower temporal correlation (∼0.5–0.6), which is due to the absence of a clear seasonal cycle in the observations, which is more pronounced in the model (see Fig. 4).

3.2.2 NO_3^-

NO_3^- is not reproduced with the same consistency as SO_4^{2-}. The model predicts the observed average nitrate concentration with a general overestimation over Europe and West USA and a strong overestimation over East Asia (see Fig. 7). Nevertheless, the seasonal cycle is generally well reproduced by the model (see Fig. 7, lower panel) both in the eastern USA (with a temporal correlation coefficient of ∼0.8–0.9) and in Japan (with a temporal correlation coefficient between

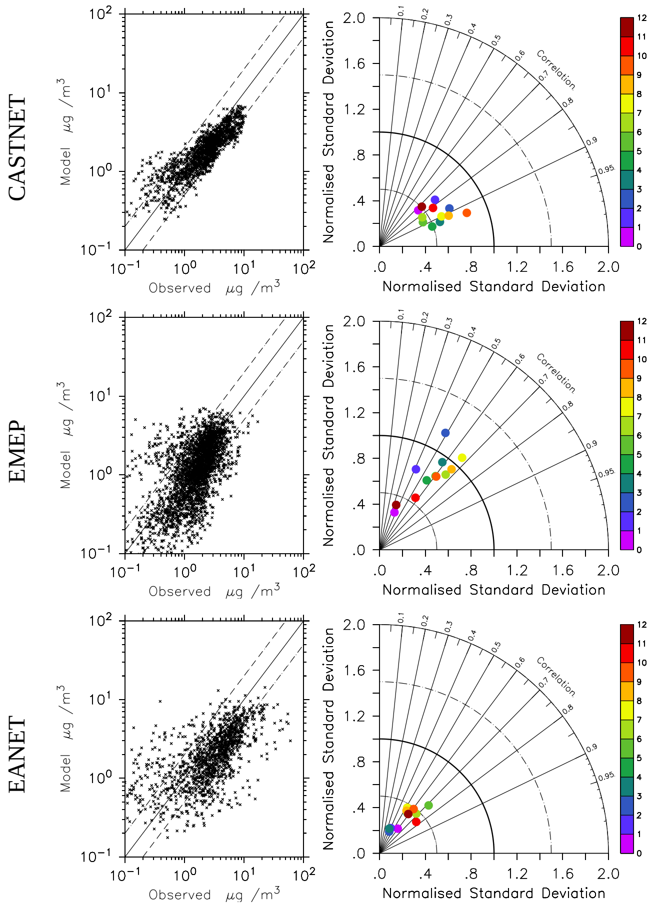

Fig. 6. Left: scatter plots of observed and modelled monthly averaged concentrations (in $\mu g\, m^{-3}$) for the year 2005–2008 of SO_4^{2-}. Right: Taylor diagram of the comparison between station observations and model results. The color code denotes the month of the year for which the statistical values are calculated. Upper: observations from CASTNET, middle: observations from EMEP, lower: observations from EANET.

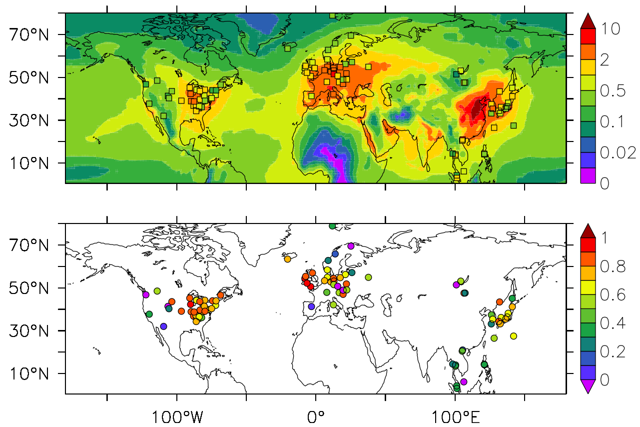

Fig. 7. As Fig. 5 but for NO_3^-.

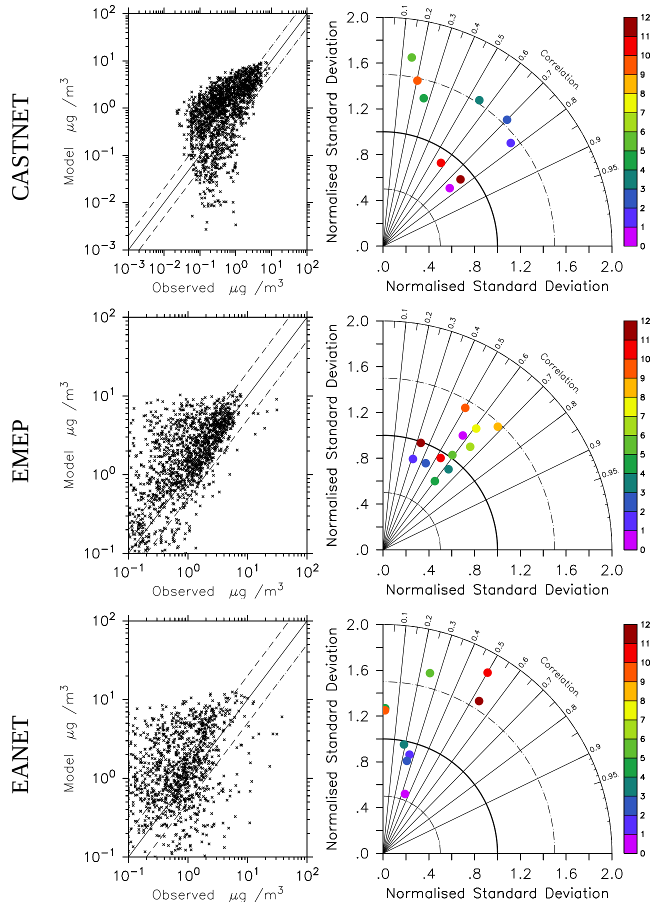

Fig. 8. As Fig. 6 but for NO_3^-.

∼0.6 and 0.8), while a somewhat lower temporal correlation is calculated for some locations in Europe and West USA. The calculated mean is ∼60 % higher than observed (see Table 3 and Fig. 8) for all networks. Additionally, the RMS is higher than the standard deviation of the observations, implying an incorrect representation by the model of this aerosol constituent. This difference between model and observations is possibly due to measurement biases in the networks. As mentioned in Sect. 2.2, the nitrate concentrations measured with teflon filters can be low biased, especially in warm and dry conditions, as nitrate evaporates from the filters (Ames and Malm, 2001). As shown by Schaap (2003), Schaap et al. (2004) and De Meij et al. (2006), NH_4^+ and NO_3^- partially evaporate from the filters at temperatures between 15 °C and 20 °C while at higher temperatures it can evaporate completely. It is therefore possible that observational biases are responsible for the limited agreement between model results and the observations. This effect is not noticeable in Fig. 4, because the concentrations of nitrate aerosols have a minimum during summer. However, a possible indication of the evaporation of nitrate from the sampling filters is presented in the Taylor diagrams in Fig. 8. In the comparison

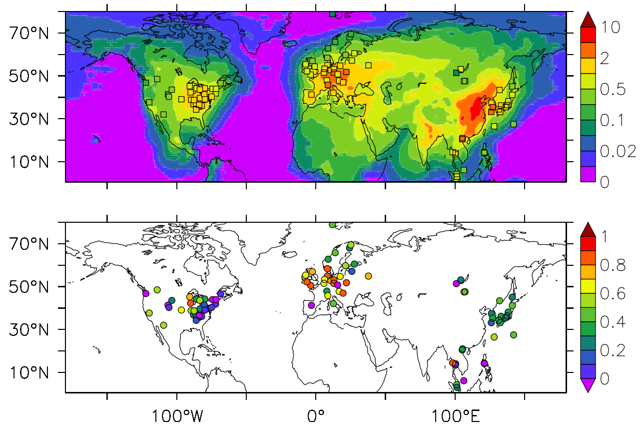

Fig. 9. As Fig. 5 but for NH_4^+.

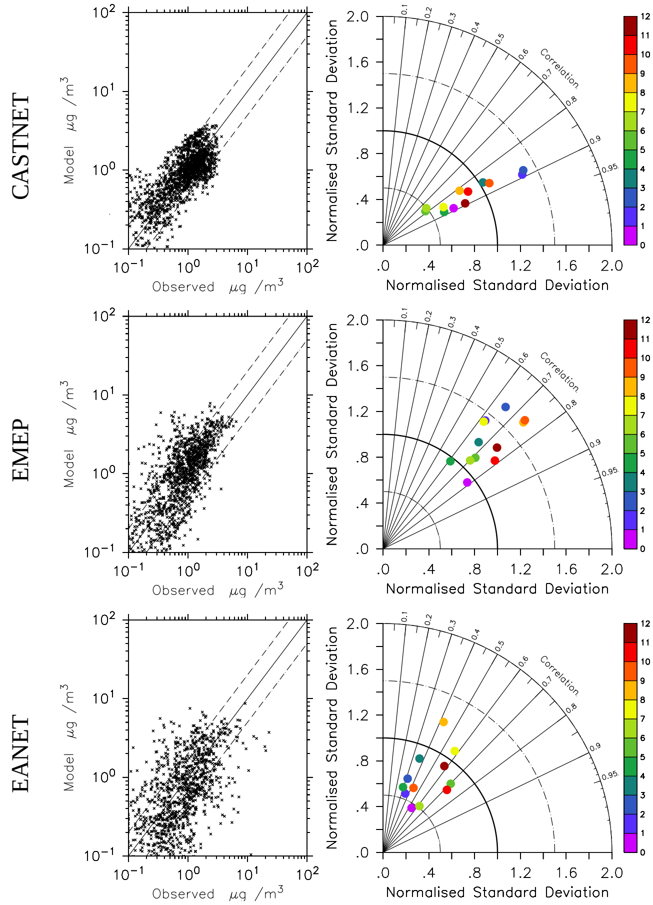

Fig. 10. As Fig. 6 but for NH_4^+.

with EANET the spatial correlation for the summer months is outside the visible diagram, indicating a strong overestimation of the model spatial variability with respect to the observations. For the colder winter period (with lower evaporation of nitrate from the filters), the model results agree much better with the observations. In the case of CASTNET observations the spatial correlation coefficient is higher than 0.7 for December–March. Similarly, the model reproduces the EANET observations' spatial distribution during November and December with a spatial correlation higher than 0.5, while the spatial correlation coefficients obtained for spring and the other winter months are between 0.2 and 0.4, but with a good normalised standard deviation (~0.5, ~0.8, ~0.9 and ~0.9 for January–April, respectively). This suggests that during winter time the amplitude of the spatial distribution is similar between model and observations though the patterns are not fully similar. Although the spatial correlation and variability agreement/disagreement cannot confirm the evaporation from the filter, it indicates that this process may play an important role. Furthermore, as mentioned in Sect. 3.2.1, particular attention has to be paid when drawing strong conclusions from a comparison with the EANET network. Nevertheless the results here obtained suggest that the spatial distribution (regardless of the bias) agrees better during winter than during summer. In addition, there is a large scatter between EANET observations and simulation results (confirmed by low time correlations in many location, see Fig. 7), caused by an overestimation of nitrate concentrations at marine sites. In contrast to the EANET observations, the model results agree well with the observed nitrate from the EMEP network, with a spatial correlation of ~0.5–0.6 and a normalised standard deviation between 0.5 and 1.5.

3.2.3 NH_4^+

As shown in Fig. 9, high NH_4^+ concentrations are predominantly found over continental regions, especially India, China and Central Europe, which agrees with the findings of Clarisse et al. (2009). The spatial distribution of NH_4^+ agrees reasonably well with the observation for all three observational networks. Excellent agreement is achieved between the model and observations of the CASTNET network, with spatial correlation coefficients higher than ~0.8 (see Fig. 10) and with 87 % of the modelled values within a factor of two of the observations (see Table 3), while some discrepancies in the spatial distribution are found over Europe and East Asia. Additionally RMS values are very close to the standard deviations of the observations, which implies a deviation of the model results from the observed concentrations of NH_4^+. As mentioned in Sect. 3.2.2, possible evaporation from the filters during summer could influence the observations. As for NO_3^-, it is difficult to quantify if this effect, as NH_4^+ concentrations are very low during the summer months. Because NH_3 emissions follow a strong seasonality, their influence on NH_4^+ formation is by far larger

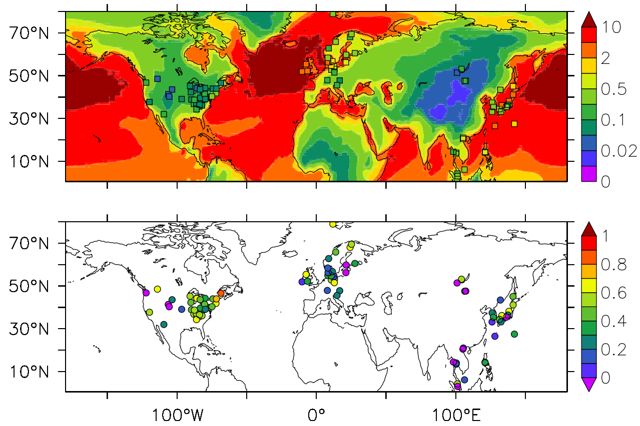

Fig. 11. As Fig. 5 but for Na^+.

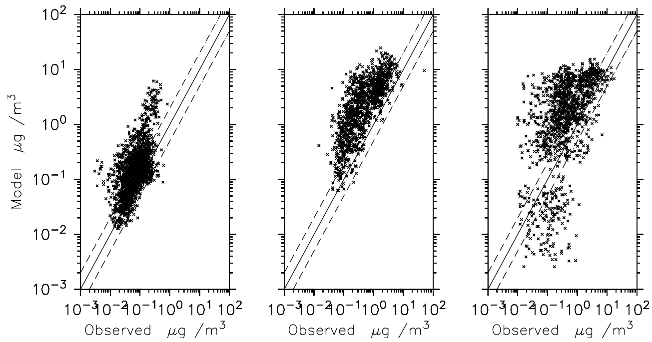

Fig. 12. Scatter plots of station observed and modelled monthly averaged concentrations (in $\mu g\,m^{-3}$) for the year 2005–2008 of Na^+. Left: observations from CASTNET, middle: observations from EMEP, right: observations from EANET.

than the possible filter evaporation. In fact, although the spatial distribution is well reproduced, some discrepancies are found for the temporal variation of NH_4^+ (see Fig. 9, lower panel). The model results and the observations correlate reasonably well over Europe and East Asia (with temporal correlations generally above 0.7 and 0.5, respectively), but the model does not achieve temporal correlations with observations over the East USA. For these locations, the model calculates a double peak in the NH_4^+ concentration during spring (March) and autumn (September). For example, for the station Edgar Evins (Tennesee, USA, 36° N–86° W, see Fig. 4) a small peak during September $\sim$1.7 $\mu g\,m^{-3}$ and a large peak of $\sim$2.5 $\mu g\,m^{-3}$ during March (monthly average) is modelled. This biannual maximum is a direct result of the seasonal cycle of the NH_3 emissions in the region, which have a clear maximum in March and a secondary peak in September. This seasonality is not seen in the observations, which show a single yearly maximum for this location around September of $\sim$2.4 $\mu g\,m^{-3}$ (monthly average). The difference for the summer months is even higher if evaporation from the filter of NH_4^+ is considered, exacerbating the difference between model results and observations. The emission database seems to reproduce the fertilizer applications (Goebes et al., 2003) over the USA, while the importance of livestock appears to be strongly underestimated. Emissions from livestock cause a yearly maximum at the end of summer and they should account for $\sim$80 % of the NH_3 emissions in the region (Battye et al., 2003). The EDGAR-CIRCE emission dataset groups both emissions sources as "agricultural" (see Doering et al., 2009a, and references therein), making it impossible to test this hypothesis and to establish the real reason of the incorrect seasonality in the emissions. A revision of the emissions for this region is recommended.

3.2.4 Sea spray and sodium

Sea spray aerosol (SS) consists mainly of chloride and sodium (Millero, 2003), which may both be used as proxies for seasalt aerosol. However, chloride can react with acidic gases like nitric acid, causing chloride loss to the gas phase (in the form of HCl) (McInnes et al., 1994). On the other hand, sodium does not evaporate and has only minor non-marine sources (White, 2008), and can be used to estimate the total SS concentration. Following the studies of Manders et al. (2010) and Millero (2003), it is estimated that around one third of sea salt mass is sodium. In this work SS has been speciated in three different components: as bulk species (14 %), as chloride (51.6 %) and as sodium (33.7 %) (see Sect. 2.1 and Pringle et al., 2010a). Hence sodium can be directly compared with observations, and the result reflects also the SS distributions.

As shown in Figs. 11 and 12, sodium is overestimated at almost all stations in the CASTNET, EMEP and EANET networks. The overestimation is more pronounced over Europe than over the USA and East Asia. The RMS values in Table 3 are consistently higher (a factor of two) than the standard deviation of the observations, indicating that the model does not correctly reproduce the observed concentrations (see also Fig. 4). Figure 12 shows that Na^+ is overestimated especially with respect to the EMEP and EANET network, while a partial (low) agreement is present with respect to the CASTNET network. On the other hand, the seasonality of the SS aerosol concentration (see Fig. 11, lower panel) is correctly reproduced over eastern USA, norther Europe and at some locations over Japan, while a low temporal correlation coefficient (below 0.4) is calculated for other stations (especially inland). Over water the total column of SS is correctly reproduced, as indicated by the accurate calculation of the AOD over oceanic areas (see Sect. 3.1). It must be mentioned that in this study, the hydrophilic coarse mode is assumed to have a geometric standard deviation (σ) of 2.2, leading to a relative high dry deposition rate and sedimentation over land. This increase in the hydrophilic coarse mode geometric standard deviation was suggested by a previous horizontally coarser numerical experiment with a similar set up of the EMAC model (Pringle et al., 2010a), which showed an overestimation of a factor of two compared to observations, analogously to that obtained by Stier et al. (2005). This overestimation is not only still present in this study, but it even increased, with a general overestimation of a factor of ∼3 (see Table 3). Hence, this study indicates that the SS overestimation is not caused by a coarse horizontal resolution (as speculated by Pringle et al., 2010a; Stier et al., 2005). However, the coarse vertical resolution might be the cause of the SS overestimation over land, as the model may be unable to capture the correct deposition and sedimentation at the lowest level. As shown by Maring et al. (2003), SS is distributed vertically following a logarithmic profile, which is very difficult to reproduce with a coarse vertical resolution, as used in EMAC (the first level is centered at ∼30 m and has a vertical extent of ∼60 m). An improved deposition function is needed in future simulations to describe the sea spray distribution more accurately.

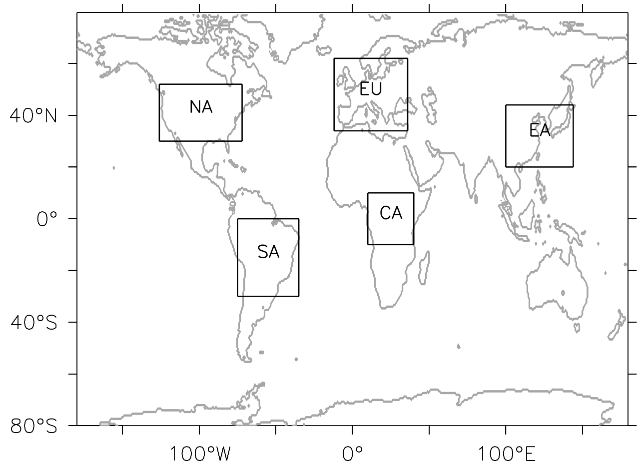

Fig. 13. Location and extension of the geographical regions used in the budget calculation. The regions are: North America (NA), Europe (EU), East Asia (EA), Central Africa (CA) and South America (SA).

4 Global and regional budgets

Because of the relatively high spatial and temporal resolution of the simulation performed in this study, global and local budgets for aerosol compounds (and precursors) can be estimated. The different contributions of the aerosol sink processes are estimated within each region (i.e. wet and dry deposition and sedimentation). The emissions are also calculated for the bulk species (DU, SS, BC and POM), while for the non bulk species, the gas phase precursors emissions have been included. Finally, for the regional budgets, the transport in (out) to (from) the region is also calculated both for the aerosols and their precursors (for non bulk species), to achieve the budget closure. In Table 4 the global budget for some species is presented. For the bulk species we obtain similar results compared to previous works. The ratio of wet deposition to total deposition (24, 30, 79 and 80 % for dust, sea salt, BC and POM, respectively) is in good agreement with the estimates of Textor et al. (2006). Furthermore, the ratio of wet to dry deposition for BC is lower than, but similar to, Jacobson (2010), i.e. 92 %. Although the burdens of dust and sea salt are about half of that reported by Textor et al. (2006), the values are well within the standard deviation estimated from the multimodel ensemble in the same work.

Emissions of SO_x, NH_3 and NO_y (108.1 Tg S yr^{-1}, 41.0 and 40.0 Tg N yr^{-1}) are similar to reported values in the literature (e.g. Pye et al., 2009; Bauer et al., 2007; Feng and Penner, 2007; Rodriguez and Dabdub, 2004). Wet deposition of SO_4^{2-} is similar to that obtained by Rodriguez and Dabdub (2004) and Pringle et al. (2010a), though it is around a factor of two larger than the estimation of Pye et al. (2009). The wet deposition of ammonium (21.0 Tg N yr^{-1}) is in agreement with the results of Pye et al. (2009) and Feng and Penner (2007). Finally, wet deposition of nitrate (18.9 Tg N yr^{-1}) is similar to that obtained by Rodriguez and Dabdub (2004), but around 25 % lower than that obtained by Pringle et al. (2010a) with the same model but different emissions. The dry deposition of the analyzed species are in line with the reported literature values.

Regional budgets were also calculated for five specific continents (see Fig. 13): Europe (EU), North America (NA), South America (SA), Central Africa (CA) and East Asia (EA). The budgets for the different regions are presented in Table 5 and graphically in Figs. 14 and 15.

As expected the largest dust burdens are present over Europe, Central Africa and East Asia. Over Europe and Central Africa the dust is imported from the surrounding regions (∼34 Tg yr^{-1} each), while in East Asia dust is locally emitted (∼46 Tg yr^{-1}). Note that dust is deposited differently in the regions: while for Europe and Central Africa wet deposition is the main sink (∼30 and ∼24 Tg yr^{-1}, respectively) compared to sedimentation (∼11 and ∼9 Tg yr^{-1}, respectively), for East Asia sedimentation is the most dominant removal mechanism, being a factor of two higher than wet deposition (∼38 and ∼17 Tg yr^{-1}, respectively). The reason for this is that near the source, the particles are removed more efficiently by sedimentation due to their large size.

For sea salt the budgets are more equivalent than for dust. In all regions sedimentation plays a major role as a sink of sea salt (see Fig. 14). The ratio of sedimentation to wet deposition ranges from ∼1.5 (in East Asia) to ∼1.9 (in North America and South America), which is in line with the ratio for the entire globe (∼1.7). The only exception is Central Africa, where sedimentation contributes only ∼0.85 to the wet deposition. This is due to the fact that almost no local emissions are present and the sea salt is entirely transported into the region. In conclusions, local emissions and sedimentation are the most important process in the sea salt budget over the open ocean and coastal areas, while, over land,

Table 4. Global aerosol budget. All units in Tg (species) yr^{-1}, except nitrogen and sulfur compounds (expressed as Tg N yr^{-1} and Tg S yr^{-1}, respectively). NO_y includes NO, NO_2, peroxyacytyl nitrate (PAN), NO_3, HNO_4 and N_2O_5, and not nitric acid and aerosol nitrate. SO_x includes SO_2, H_2SO_4 and DMS, and not aerosol sulfate. The yearly standard deviation is listed in parenthesis.

	Emissions		Dry deposition		Sedimentation		Wet deposition		Burden	
DU	1659.3	(12.6)	65.3	(3.1)	1183.5	(18.5)	403.3	(11.1)	10.6	(0.3)
SS	7843.9	(50.0)	1422.8	(25.7)	4090.7	(13.4)	2314.3	(13.5)	5.8	(0.3)
BC	8.1	(0.1)	0.8	(0.0)	0.8	(0.0)	6.2	(0.1)	0.1	(0.0)
POM	63.4	(0.5)	6.1	(0.1)	6.1	(0.1)	50.0	(0.6)	1.0	(0.0)
NH_3	41.0	(0.2)	16.3	(0.1)	–		–		0.1	(0.0)
NH_4^+	–		0.9	(0.0)	2.6	(0.1)	21.0	(0.2)	0.1	(0.0)
SO_x	108.1	(0.9)	26.0	(0.2)	–		–		0.6	(0.0)
SO_4^{2-}	2.1	(0.0)	6.2	(0.1)	23.8	(0.2)	55.0	(0.5)	0.3	(0.0)
NO_y	40.0	(0.2)	4.4	(0.0)	–		–		2.0	(0.1)
HNO_3	–		9.8	(0.1)	–		–		1.1	(0.0)
NO_3^-	–		1.0	(0.0)	6.7	(0.1)	18.9	(0.2)	0.1	(0.0)

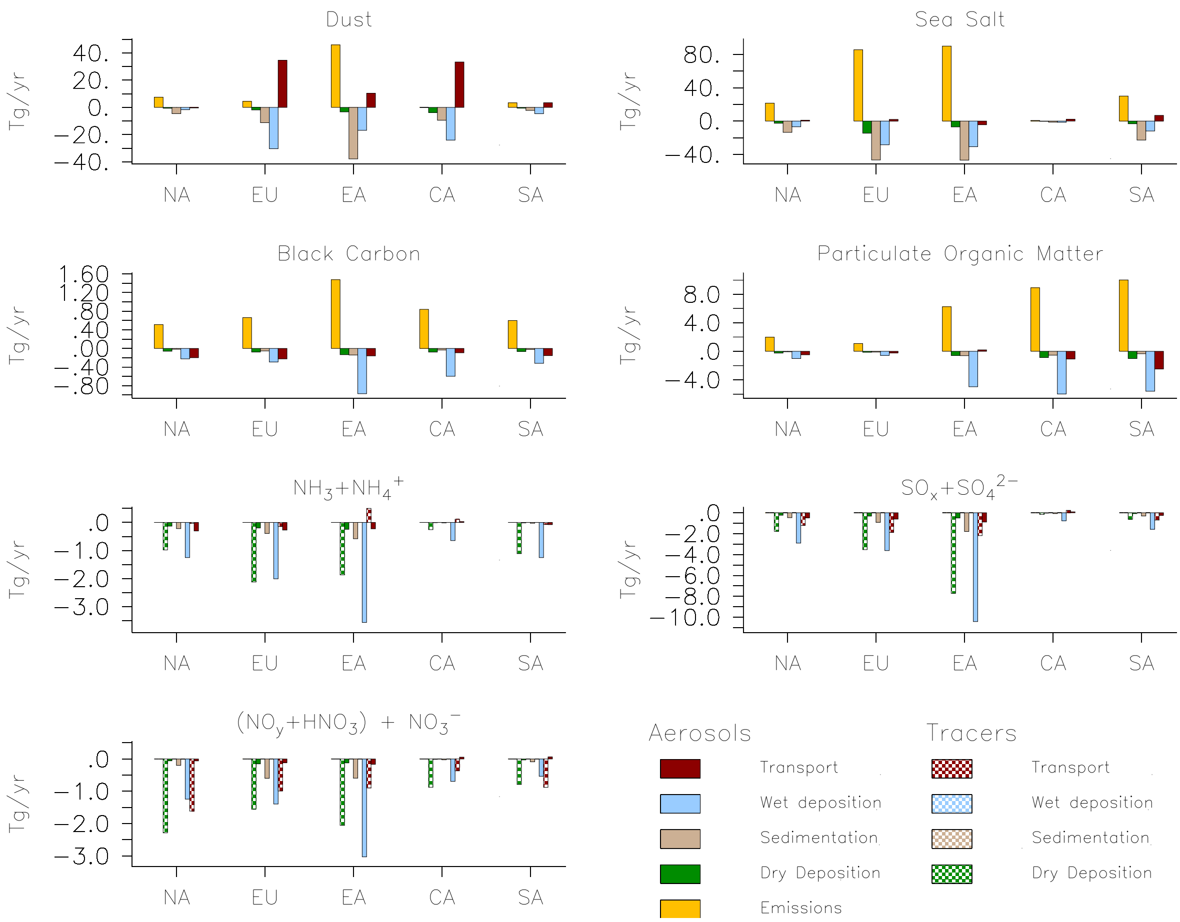

Fig. 14. Budget of different aerosol (and precursors) species as in Table 5. The colour code denotes the process, while the positive (negative) value is associated with a source (sink) of the component. Under the abscissa the regions are listed: North America (NA), Europe (EU), East Asia (EA), Central Africa (CA) and South America (SA). For non bulk species the gas-phase and aerosol contribution to the budget are also shown with dashed and solid colour bars, respectively. For the non bulk aerosol species the emissions were removed for clarity.

Table 5. Regional aerosol budgets. All units in Gg(species) yr^{-1}, except nitrogen and sulfur compounds (expressed as Gg N yr^{-1} and Gg S yr^{-1}, respectively) and the species are as in Table 4. The transport is positive (negative) associated with a net import (export) to (from) the region. The yearly standard deviation is listed in parenthesis.

	Emissions		Dry deposition		Sedimentation		Wet deposition		Transport		Burden	
					North America (126–72° W and 30–52° N)							
DU	7505.0	(63.8)	622.1	(38.4)	4569.7	(72.9)	1707.5	(89.1)	−385.6	(83.4)	32.1	(1.1)
SS	21524.3	(221.7)	2613.1	(149.9)	13551.4	(313.8)	6852.2	(243.1)	987.0	(342.2)	29.2	(1.7)
BC	511.7	(4.7)	59.7	(1.1)	17.7	(0.8)	223.5	(4.3)	−198.9	(7.2)	4.8	(0.2)
POM	1986.2	(84.6)	248.5	(9.6)	64.3	(4.2)	1010.7	(35.7)	−489.2	(72.3)	22.3	(1.6)
NH_3	2972.8	(11.6)	980.2	(18.8)	–		0.0	(0.0)	−35.7	(21.6)	7.9	(0.3)
NH_4^+	–		131.6	(4.9)	219.4	(16.0)	1251.8	(23.0)	−303.8	(11.6)	8.4	(0.3)
SOx	7336.4	(63.3)	1776.5	(43.9)	–		–		−1216.9	(111.0)	33.4	(0.3)
SO_4^{2-}	181.3	(1.3)	237.2	(10.9)	469.2	(22.8)	2904.9	(71.8)	−486.1	(23.4)	13.2	(0.5)
NO_y	5699.4	(38.3)	582.7	(21.4)	–		–		−987.7	(160.4)	66.3	(1.7)
HNO_3	–		1703.8	(19.9)	–		2.6	(0.4)	−625.0	(97.4)	35.2	(0.5)
NO_3^-	–		56.4	(2.6)	197.2	(5.0)	1242.5	(17.8)	−59.7	(7.9)	2.2	(0.1)
					Europe (12° W–36° E and 34–62° N)							
DU	4459.9	(18.8)	1856.4	(168.7)	11210.7	(823.2)	30349.2	(2234.5)	34616.7	(3581.8)	386.0	(29.0)
SS	85557.5	(912.9)	14544.0	(517.8)	46657.7	(1078.2)	28457.0	(1406.6)	2007.0	(670.2)	80.8	(2.0)
BC	662.0	(5.5)	76.6	(1.0)	53.3	(2.2)	290.5	(5.6)	−224.7	(7.5)	5.4	(0.1)
POM	1091.8	(26.8)	136.9	(3.3)	98.6	(3.0)	580.8	(24.8)	−214.2	(25.5)	12.2	(0.5)
NH_3	5261.0	(19.3)	2122.8	(42.6)	–		0.2	(0.0)	−147.0	(7.5)	7.8	(0.4)
NH_4^+	–		197.1	(4.4)	391.8	(37.5)	2008.6	(78.6)	−271.1	(8.9)	8.9	(0.5)
SOx	11232.3	(92.2)	3530.3	(37.7)	–		–		−1884.6	(119.4)	45.5	(0.7)
SO_4^{2-}	273.8	(1.9)	320.3	(3.2)	917.5	(38.2)	3620.3	(47.9)	−607.5	(26.0)	16.4	(0.7)
NO_y	5058.4	(32.5)	634.5	(11.2)	–		–		−576.4	(160.6)	68.8	(1.6)
HNO_3	–		920.9	(17.4)	–		–		−415.6	(120.4)	36.7	(0.7)
NO_3^-	–		150.9	(5.0)	597.2	(25.6)	1394.2	(40.2)	−115.1	(7.2)	3.7	(0.1)
					East Asia (100–144° E and 20–44° N)							
DU	45933.8	(309.1)	3294.9	(116.1)	37822.6	(398.7)	16845.0	(800.4)	10354.2	(1099.9)	351.4	(11.2)
SS	89937.5	(886.3)	7016.6	(421.5)	46863.3	(1272.1)	30749.6	(730.0)	−4424.2	(619.9)	96.3	(4.5)
BC	1476.6	(15.2)	133.9	(0.8)	140.5	(3.7)	972.2	(26.7)	−159.8	(23.3)	15.3	(0.3)
POM	6263.3	(70.1)	594.6	(7.9)	612.3	(12.9)	4976.6	(198.7)	201.3	(142.7)	77.0	(2.5)
NH_3	6097.2	(23.1)	1868.5	(13.5)	–		0.1	(0.0)	501.4	(61.5)	12.8	(0.3)
NH_4^+	–		244.9	(7.1)	580.3	(23.5)	3563.1	(75.5)	−226.7	(45.4)	20.7	(0.4)
SOx	23935.0	(201.6)	7715.1	(96.0)	–		–		−2187.1	(186.2)	93.7	(1.8)
SO_4^{2-}	591.2	(4.3)	502.4	(15.5)	1790.9	(38.2)	10413.7	(140.4)	−889.2	(59.9)	31.8	(0.8)
NO_y	7262.6	(49.2)	645.1	(9.2)	–		–		−568.3	(163.4)	66.0	(1.5)
HNO_3	–		1407.8	(29.3)	–		1.2	(0.1)	−330.1	(140.0)	34.9	(1.0)
NO_3^-	–		121.1	(5.6)	594.0	(12.9)	3028.7	(48.1)	−164.5	(17.4)	7.0	(0.2)
					Central Africa (10–40° E and 10° S–10° N)							
DU	3.5	(0.3)	3762.6	(552.4)	9418.7	(986.7)	24017.1	(1431.9)	33347.4	(2650.8)	327.2	(43.6)
SS	713.3	(5.2)	321.1	(5.5)	1245.0	(8.1)	1470.5	(70.9)	2182.6	(88.6)	17.8	(0.6)
BC	839.7	(31.8)	78.1	(1.3)	32.3	(1.6)	597.8	(42.7)	−93.3	(23.2)	13.0	(0.5)
POM	8928.1	(324.2)	870.3	(14.5)	543.2	(29.0)	5990.5	(422.4)	−1079.8	(228.2)	119.0	(4.3)
NH_3	761.8	(4.9)	256.8	(16.3)	–		0.0	(0.0)	116.1	(11.2)	3.8	(0.3)
NH_4^+	–		8.6	(0.5)	14.8	(1.0)	646.4	(19.7)	31.0	(7.9)	1.9	(0.1)
SOx	708.6	(15.2)	160.5	(8.1)	–		–		230.7	(15.2)	4.8	(0.2)
SO_4^{2-}	18.5	(0.4)	36.9	(1.5)	80.7	(2.9)	768.8	(34.8)	87.5	(16.1)	5.4	(0.3)
NO_y	2115.7	(68.1)	203.8	(13.5)	–		–		−361.7	(139.8)	35.2	(1.5)
HNO_3	–		670.9	(8.5)	–		0.1	(0.0)	−6.2	(74.8)	16.2	(0.8)
NO_3^-	–		9.1	(0.5)	24.2	(1.8)	692.0	(65.6)	56.8	(4.5)	0.7	(0.0)

Table 5. Continued.

	Emissions		Dry deposition		Sedimentation		Wet deposition		Transport		Burden	
South America (75° W–35° W and 30° S–0° N)												
DU	3382.4	(15.4)	472.7	(61.1)	2218.3	(32.5)	4630.4	(563.7)	3422.3	(577.9)	38.0	(4.0)
SS	30004.4	(163.4)	3230.5	(150.5)	22772.9	(196.4)	11909.4	(590.2)	6823.9	(599.2)	68.8	(1.6)
BC	599.4	(103.2)	64.3	(11.8)	21.6	(6.3)	319.7	(65.6)	−154.0	(24.2)	8.1	(1.7)
POM	10020.4	(1144.5)	1012.7	(129.3)	339.8	(96.2)	5603.7	(898.4)	−2484.2	(341.9)	117.5	(15.8)
NH_3	2606.4	(16.7)	1110.2	(14.9)	–		–		−73.4	(32.7)	7.7	(1.0)
NH_4^+	–		15.3	(1.7)	29.0	(3.1)	1252.2	(56.0)	−77.7	(13.3)	2.3	(0.2)
SOx	3827.7	(60.7)	625.5	(6.8)	–		–		−703.6	(117.8)	20.9	(0.2)
SO_4^{2-}	91.2	(1.4)	84.3	(5.2)	309.9	(10.6)	1582.8	(123.2)	−245.2	(27.3)	9.7	(0.6)
NO_y	2576.2	(210.0)	320.0	(19.4)	–		–		−807.9	(170.9)	62.6	(2.9)
HNO_3	–		467.8	(102.1)	–		0.2	(0.0)	−69.6	(134.7)	22.1	(1.5)
NO_3^-	–		29.3	(2.3)	86.7	(3.5)	534.3	(79.2)	62.5	(6.8)	1.5	(0.1)

wet deposition is a more effective sink than the sedimentation. Sea salt is similar to dust in that near the source regions coarse mode particles are the biggest contributors to the total sea salt mass. These particles are removed efficiently by sedimentation, while far from the local sources small particles, which are more efficiently removed by wet deposition, are the main contributor to the burden.

Black carbon, in contrast to sea salt and dust, shows interesting differences between the different regions. In general wet deposition is the main removal process for this compound, being an order of magnitude more important than sedimentation and dry deposition. In some regions transport of BC is also essential as removal term: e.g. in North America, Europe and South America the removal by transport is of a similar magnitude to the sink from wet deposition. For East Asia and Central Africa transport plays only a minor role, comparable to dry deposition and sedimentation. For East Asia, the small contribution of transport is due to the relatively stagnant dynamical conditions, especially outside the monsoon season (Lawrence et al., 2007). Hence, for black carbon the importance of the atmosphere dynamics should be underlined, as well as the importance of the selected region boundaries. Furthermore, for East Asia, the strongly polluted conditions allow a very effective conversion from hydrophobic to hydrophilic particles within the region (Ma et al., 2010).

For POM we see that Central Africa and South America are strong exporters (∼1.1 and 2.4 Tg (POM) yr^{-1}, respectively), due to the vegetation emissions and strong biomass burning events in these regions (see Fig. 15). As for BC, wet deposition is the main sink term for all regions, while sedimentation plays a much smaller role, due to the small size of POM on emission (Aitken mode). The ratio of sedimentation to wet deposition is similar in all regions, ranging from ∼0.06 (in North America and South America) to ∼0.16 (in Europe), and it is similar to the global value of ∼0.12.

In general, the ammonia emissions are very large over industrialised/agricultural regions and the ammonium aerosol distribution closely reflects the emissions (see Sect. 3.2.3). Dry deposition of NH_3 and wet deposition of NH_4^+ are of the same magnitude in North America (∼0.9 and ∼1.2 Tg N yr^{-1}, respectively), Europe (∼2.1 and ∼2.0 Tg N yr^{-1}, respectively) and South America (∼1.1 and ∼1.2 Tg N yr^{-1}, respectively). In contrast, wet deposition of NH_4^+ is a factor of two higher than wet deposition of NH_4^+ in East Asia (∼1.8 and ∼3.5 Tg N yr^{-1}, respectively) and Central Africa (∼0.2 and ∼0.6 Tg N yr^{-1}, respectively). The East Asia region covers a large portion of ocean area, where dry deposition of NH_3 is less important when compared to land areas. This leads to a large burden of NH_3 and NH_4^+, which is finally removed via wet deposition. In fact, while Europe and East Asia have similar emissions, the Asian burden of NH_3 is almost a factor of two higher (∼8 and ∼13 Tg N for Europe and East Asia, respectively), with even larger differences in the NH_4^+ burden (∼9 and ∼21 Tg N for Europe and East Asia, respectively). In contrast to East Asia, Central Africa is characterized by a relatively strong contribution from wet deposition due to the stronger transport contribution for NH_3 and NH_4^+ (∼20 % of the emissions). The vertical profiles of NH_3 indicate that ∼75 % of the tracer burden occurs above the surface layer, while for the other regions this is ∼60 %.

Sulfate aerosol has the largest burden over industrialised regions (Europe, North America and East Asia), and it is at least a factor of 2 lower over Central Africa and South America. East Asia is clearly a strong exporter of sulfate, with around ∼34 % of the global anthropogenic SO_2 emissions (and ∼25 % of the total SO_x emission) being concentrated in the region. Although the SO_x emissions (∼24 Tg S yr^{-1}) are more than twice the emissions in Europe (∼11 Tg S yr^{-1}), most of the sulfur is converted to sulfate and washed out within the region. This leads to an export of ∼2.2 Tg S yr^{-1}

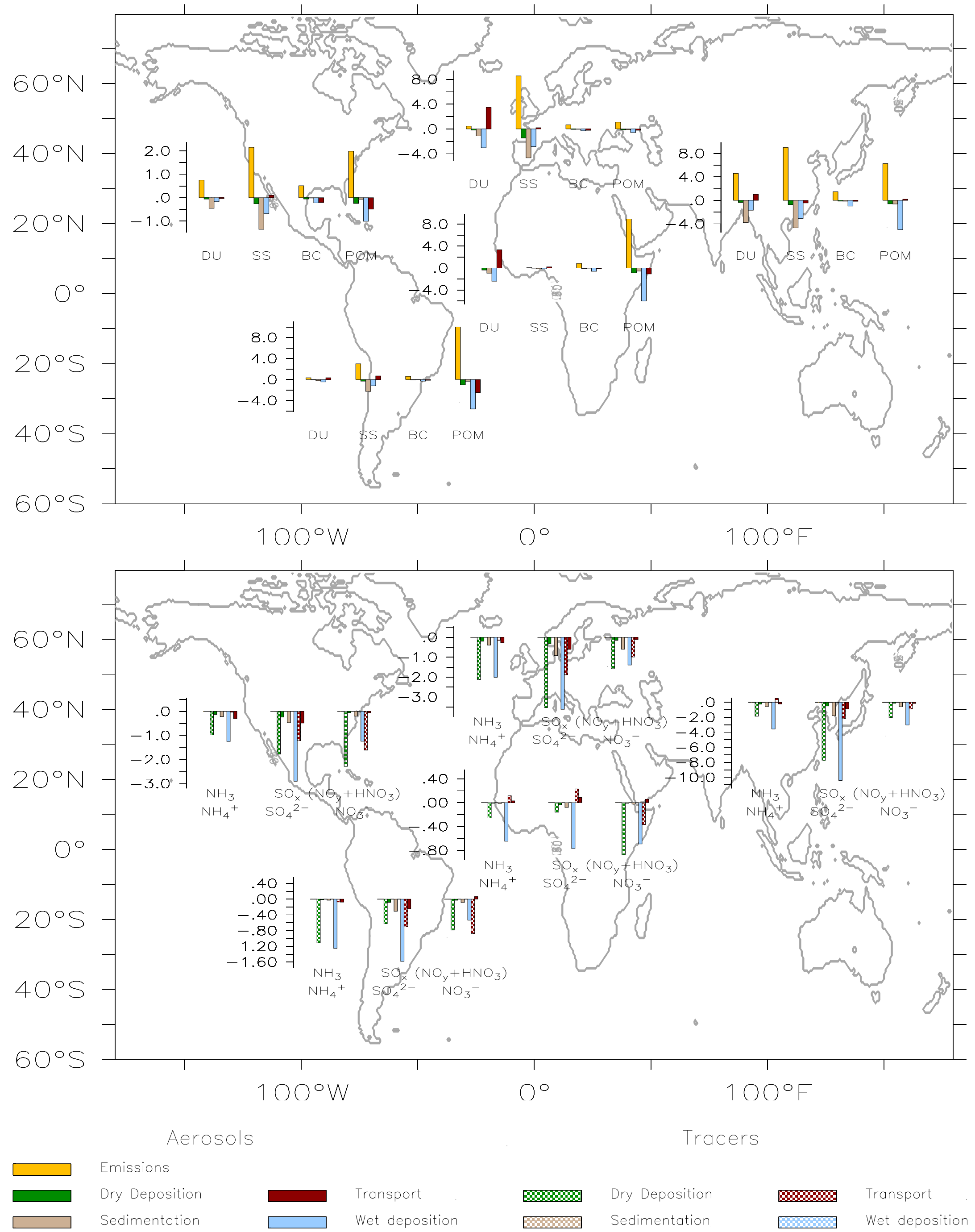

Fig. 15. Budget of different aerosol (and precursors) species as in Table 5, displayed by regions. The colour code denotes the process while the positive (negative) value is associated with a source (sink) of the component. Under the abscissa the components are listed: dust (DU), sea salt (SS), black carbon (BC) and particulate organic matter (POM). The units are all in $Tg\,yr^{-1}$ (TOP) and in $Gg\,N\,yr^{-1}$ and $Gg\,S\,yr^{-1}$ (BOTTOM). DU and SS are reduced by a factor of 10 for clarity. For the non bulk aerosol species the emissions were removed for clarity. Please note the different vertical axis in each diagram.

which is comparable to that from Europe ($\sim$1.9 $Tg\,S\,yr^{-1}$). This indicates again that transport in (out) from the selected region for East Asia is not as effective as in the other regions considered. South America (mainly the Amazon basin) is a largely pristine region with highly localised industrial activities. The sulfate aerosol burden is much lower compared to industrialised regions, though it is around a factor of 5 higher than for Central Africa.

For nitrate aerosol three main processes balance the emissions within each region: the wet deposition of NO_3^-, the transport from the region of NO_y and the dry deposition of $NO_y + HNO_3$. Depending on the region selected and the associated outflow conditions of the precursors, the other two terms (mostly) balance the emissions. East Asia and North America appear to represent two extreme cases. In North America the outflow towards the Atlantic ocean removes a large amount of $NO_y + HNO_3$ ($\sim$1.3 Tg N yr^{-1}), corresponding to $\sim$30 % of the total $NO_y + HNO_3 + NO_3^-$ removal. The removal of these quantities of precursors lead to a reduced formation of NO_3^- and, in turn, a lower removal by wet deposition of NO_3^- ($\sim$1.2 Tg N yr^{-1}, or 20 % of the total removal). In contrast, the East Asian outflow of $NO_y + HNO_3$ ($\sim$0.9 Tg N yr^{-1}, i.e. 12 % of the total removal) is small, and nitrogen compounds can be converted within the region, leading to higher NO_3^- wet deposition ($\sim$3 Tg N yr^{-1}, or 45 % of the total removal). Finally, the case of Central Africa is quite interesting and unique. This relatively clean and pristine region is a net importer of most of the compounds considered here, with the exception of NO_y, which is emitted from biogenic sources and by biomass burning ($\sim$0.5 and 1.2 Tg N yr^{-1}, respectively). Similarly to Central Africa, the South American continent also exports nitrogen compounds ($\sim$0.8 Tg N yr^{-1}), due to biogenic and biomass burning emissions.

5 Effect of monthly distribution of anthropogenic emissions

As mentioned in Sect. 2.1.1, the EDGAR-CIRCE inventory accounts for emissions on a relatively high spatial resolution with monthly temporal variation. To evaluate the impact of the temporal distribution on the calculated aerosol concentrations, an additional model simulation (named NS, No Seasonality) was performed and the results were compared with the calculated concentrations of the standard simulation described in this work (here named ST, STandard case). Due to the large computational requirement for these simulations, simulation NS covers only the year 2005. This year is expected to be represented by the model with the highest consistency, mainly because the chosen emissions of primarily emitted species was compiled for this year. 2005 is also meteorologically representative, without major annular mode such as the El Ñino Southern Oscillation and the North Atlantic Oscillation. The model set-up of simulation NS is the same as simulation ST (described in Sect. 2.1), but without the monthly distribution of the anthropogenic components, i.e. neglecting the seasonal cycle present in the EDGAR-CIRCE database. Hence, the annual total emissions are the same.

Because no coupling between the radiation and the atmospheric composition was active in the simulations, the nudging forces the model with the same intensity both in ST and the NT simulations. More specifically the dynamics (and the transport) in both simulations are binary identical. Hence, the differences in the aerosols (and precursors) concentrations (mixing ratios) between simulation ST and NS calculated by the model are entirely due to the different emissions and not to different meteorology.

In Table 6 the results of NS and ST are compared with observations for different aerosol species for the year 2005. For SO_4^{2-} the calculated yearly averages by NS indicates a low bias relative to the observations compared to ST, while for all other species ST represents the yearly average better.

In general the RMS is very similar in both simulations, with the only substantial difference being for NO_3^-, where simulation ST performs better than NS, as indicated by the comparison to EMEP and CASTNET observations. Nevertheless, the RMS is in these cases is higher than the standard deviation of the observations, implying that the model still deviates from the observed values.

The comparison of SO_4^{2-}, NO_3^-, and Na^+ with the EANET network does not show significant differences between the two simulations. This is due to the small seasonal cycle present in the EDGAR-CIRCE data for East Asia (see also Fig. 4). For example, SO_2 emissions in China do not have a strong seasonal cycle (Zhang et al., 2009), because of the continual energy production for industry and domestic usage. Therefore, neglecting the seasonal cycle hardly affects the calculated concentrations in this region. The comparison of model results from simulations NS and ST with CASTNET observations suggests larger differences, especially for SO_4^{2-}. The bias and the RMS is smaller for NS than ST when compared to the observations. This is caused by the strong monthly variability in the SO_2 emissions over the USA. The SO_2 emissions show a difference of a factor of 2 between winter and summer emissions (being lower in summer). Photochemical oxidation is a very important source of aerosol formation which contributes more than 50 % to the SO_4^{2-}, and this is larger in summer than winter. In NS, the SO_2 emissions are higher in the summer than in ST, which leads to higher SO_4^{2-} concentrations. SO_4^{2-} concentrations are then further enhanced by the efficient photochemical oxidation of SO_2 that occurs in summer. During winter, lower emissions of SO_2 in NS do not influence the calculated SO_4^{2-} concentrations, because of the reduced photochemical oxidation. This can be seen in Fig. 16 (left) where the summer concentrations for SO_4^{2-} are higher than during winter. Analogously, this effect is also observed for NO_3^- concentrations and the related NO_x emissions (although less strongly); also in this case, the yearly average is somewhat higher in simulation NS than in ST, especially when compared to CASTNET. The temporal correlation of NS with the observations is somewhat lower than for ST, with a decrease of $\sim$10 % for SO_4^{2-} and 5% for NO_3^-, depending on the station.

In contrast to SO_4^{2-} and NO_3^-, the concentrations of NH_4^+ depend mainly on the sources of NH_3, emitted by

Table 6. Summary of the comparison of model results to observations of aerosol concentrations. OAM and MAM are the arithmetic mean of the observations and of the model, respectively (in $\mu g\,m^{-3}$), while OSTD and MSTD are the standard deviation of the observations and of the model, respectively (in $\mu g\,m^{-3}$). Bias represents the difference between MAM and OAM. MAM and MSTD were calculated sampling the model at the locations of the observations and monthly averaged as the observations, for the 2005–2008 period. MAM, OAM, MSTD and OSTD represents co-located measurements and model results. PF2 is the percentage of modelled point within a factor of two of the observations. RMS denotes the Root Mean Square error.

					ST					NS					PF2 difference
Species	Network	n. stations	OAM	OSTD	MAM	MSTD	Bias	PF2	RMS	MAM	MSTD	Bias	PF2	RMS	PF2(ST) – PF2(NS)
SO_4^{2-}	CASTNET	32	2.9	2.0	2.0	1.2	−0.8	94.7	1.1	2.2	1.5	−0.6	94.2	1.0	0.5
SO_4^{2-}	EMEP	58	1.9	1.3	1.6	1.2	−0.5	94.0	1.2	1.7	1.1	−0.4	92.7	1.2	1.3
SO_4^{2-}	EANET	27	4.4	5.3	2.4	1.9	−2.1	92.3	4.8	2.4	1.9	−2.1	91.7	4.8	0.6
NO_3^-	CASTNET	32	0.9	1.0	1.7	1.6	0.9	42.6	1.2	1.9	1.8	1.1	40.1	1.4	2.5
NO_3^-	EMEP	31	1.6	1.6	2.7	2.3	1.0	66.1	1.8	2.7	2.2	1.0	66.1	1.9	0.0
NO_3^-	EANET	26	1.2	1.9	1.9	2.0	0.7	52.5	2.1	1.9	2.0	0.7	53.1	2.1	−0.6
NH_4^+	CASTNET	32	1.0	0.6	1.0	0.6	0.0	86.8	0.5	1.1	0.6	0.1	83.2	0.5	3.6
NH_4^+	EMEP	30	0.9	0.9	1.3	1.2	0.2	82.7	0.8	1.4	1.2	0.3	78.4	0.9	4.3
NH_4^+	EANET	26	1.1	1.4	0.9	1.0	−0.2	86.1	1.2	0.9	1.0	−0.2	85.1	1.1	0.9
Na^+	CASTNET	32	0.1	0.1	0.3	0.6	0.2	43.4	0.6	0.3	0.6	0.2	42.6	0.6	0.8
Na^+	EMEP	24	0.9	3.1	3.6	3.5	2.6	13.5	3.9	3.7	3.5	2.7	13.5	3.9	0.0
Na^+	EANET	26	1.0	1.5	2.9	2.9	1.9	36.3	2.5	2.9	2.9	1.9	36.0	2.5	0.3

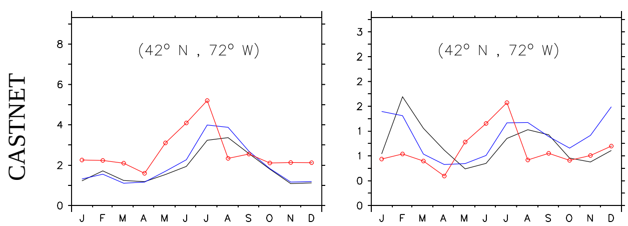

Fig. 16. Comparison of simulated and observed SO_4^{2-} (left), and NH_4^+ (right) concentrations (in $\mu g\,m^{-3}$) for a selected location of the CASTNET observational network. The red lines represent the observations, while the simulated monthly averages are indicated by the black and blue lines for simulation ST and NS respectively. The location of the station (longitude and latitude) is indicated. Note the different scales of the vertical axes.

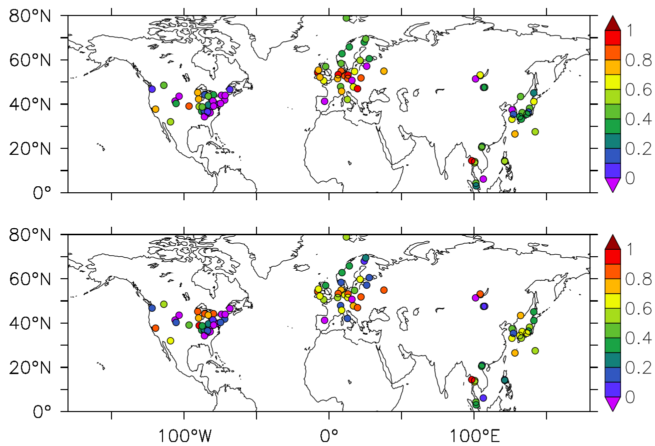

Fig. 17. Temporal correlation of observations from CASTNET, EMEP and EANET and model results for the year 2005 of NH_4^+. Upper: model results from simulation ST; lower: model results from simulation NS.

livestock and fertiliser usage, which are higher during the spring/summer months because of the intense agricultural activities. Ignoring the temporal distribution of NH_3 emissions in NS shows a strong impact on the calculated NH_4^+ concentrations and confirms the findings by De Meij et al. (2006) and Schaap et al. (2004). Calculated NH_4^+ concentrations by ST show a smaller bias than NS (see Table 6) and the model percentages of agreement within a factor of two to the observations, are higher for ST than NS with 3.6, 4.3 and 0.9 % increase when compared to CASTNET, EMEP and EANET, respectively. The improved agreement between observations and model results of simulation ST with respect to simulation NS is mostly noticeable when comparing model results with measurements from the EMEP network. In this case the model average from simulation ST (1.3 $\mu g\,m^{-3}$) is closer to the observed (0.9 $\mu g\,m^{-3}$) than the model average from simulation NS (1.4 $\mu g\,m^{-3}$), but also the RMS is lower for simulation ST than for simulation NS (0.8 and 0.9 $\mu g\,m^{-3}$, respectively). Further, as shown in Fig. 17, the temporal correlation between model results and EMEP and EANET observations generally decreases (∼10 %) when the temporal distribution of the NH_3 emissions is ignored. It is interesting to see that NS correlates better with CASTNET than ST (see also Fig. 16). As mentioned earlier, this may be related to the dual peak in the seasonal cycle of the NH_3 emissions not present in the observations (see Sect. 3.2.3). The lack of seasonality in NS improves the temporal correlation for many stations especially in the eastern part of the USA, although it remains rather low for many stations.

The spatial correlation coefficients between model results and observations show only small differences (between the ST and NS simulations) for all aerosol species included in this study. The reason is that the overall spatial distribution of the emissions does not change between the two simulations; it shows the same patterns over the year. Finally, the impact of changing the monthly distribution on Na^+ concentrations is negligible. The reason for this is that the main emission source of Na^+ is mostly natural (i.e. sea spray) and therefore calculated concentrations do not change between the two simulations.

6 Conclusions

The newly developed global anthropogenic emission inventory (EDGAR-CIRCE) of pollutant gas and aerosol emissions has been incorporated in to the chemistry general circulation model EMAC (ECHAM5/MESSy Atmospheric Chemistry). Model results covering the years 2005–2008 were compared with observations from satellites and regional networks to evaluate the results. The calculated AODs agree well with the satellite observations (level 3 products) over most of the globe, with negative biases in equatorial areas and in the dust outflow regions (i.e. Central Atlantic and Northern Indian Ocean). This is due to an underestimation of biomass burning and aeolian dust emissions. The AOD over industrialised regions is well reproduced although with some overestimation over East Asia and an underestimation near the west coast of the USA. Because the level 3 products do not include information about the sampling time, a more detailed study of the AOD produced by the model would be helpful, especially in comparison with level 2 products (i.e. with higher spatial and temporal resolution) to estimate the correct timing of pollution episodes and to quantify in more detail the simulation quality over industrialised regions.

Compared to regional network observations of aerosols, the model reproduces the main spatial and temporal atmospheric distribution of the sulfate, ammonium and nitrate aerosols. More specifically, good agreement is found for the simulated spatial distribution of sulfate and ammonium, while nitrate shows some differences when compared to observations. The temporal development of these aerosol species are in line with measurements, with the exception of ammonium aerosol, which shows some deviations from observations over the USA, mainly due to incorrect emissions of ammonia from livestock in the inventory. Finally, sodium, used as a proxy for the sea spray aerosol, shows an overestimation, previously seen with similar models, which may be related to a lack of detail in the representation of gradients in coastal regions, requiring improved emission and deposition parametrizations.

Aerosol and precursors budgets (i.e. emissions and sink terms) for five different regions (North America, Europe, East Asia, Central Africa and South America) were estimated based on the model results. The different meteorological regimes of the regions are central in explaining the different relative contribution of the sink terms to the budget. It is found that over East Asia nitrate and sulfate aerosol precursors are largely converted and transferred into the aerosol phase and efficiently removed via wet deposition. This effect is reduced in North America and Europe, where transport of precursors out of the region is an important contribution to the removal processes. For the bulk species it is found that sedimentation plays an important role for dust and sea salt if the regions encompass sources of such aerosols, since the mass of the emissions is dominated by the coarse mode. In contrast, for black carbon and particulate organic matter wet deposition plays a major role in the budget, as the these aerosols are mostly emitted in the Aitken mode.

The use of monthly varying anthropogenic emissions improves the model ability to reproduce the observations compared to annual mean emissions, with an improved temporal correlation of 5 to 10 %, depending on the aerosol type and the location. The only exception appears for NH_4^+, for which neglecting the seasonal cycle improved the simulation results over the USA, partially correcting the incorrect seasonal distribution of the emissions. This improvement is, however, limited to the USA; in the other regions a degradation of the model results compared to the observations is obtained.

In conclusion, the emission database EDGAR-CIRCE is found to be a valuable inventory for tropospheric chemistry and aerosol studies, with only a minor issue in the emission of ammonia in the Eastern USA, and its use can be encouraged to the atmospheric chemistry community.

Acknowledgements. We thank S.Metzger for his contribution to the gmXe code. We thank the DEISA Consortium (www.deisa.eu), co-funded through the EU FP6 project RI-031513 and the FP7 project RI-222919, for support within the DEISA Extreme Computing Initiative. The simulations for this study have been performed in the DEISA grid. The research leading to these results has received funding from the European Research Council under the European Union's Seventh Framework Programme (FP7/2007–2013)/ ERC grand agreement no. 226144. We acknowledge the usage of data from the CIRCE project (contract number 036961). The authors wish also to acknowledge the use of the Ferret program for analysis and graphics in this paper. Ferret is a product of NOAA's Pacific Marine Environmental Laboratory (information is available at http://www.ferret.noaa.gov).

The service charges for this open access publication
have been covered by the Max Planck Society.

Edited by: M. C. Facchini

References

Aan de Brugh, J. M. J., Schaap, M., Vignati, E., Dentener, F., Kahnert, M., Sofiev, M., Huijnen, V., and Krol, M. C.: The European aerosol budget in 2006, Atmos. Chem. Phys., 11, 1117–1139, doi:10.5194/acp-11-1117-2011, 2011.

Asia Center for Air Pollution Research (ACAP): Eanet data on the acid deposition in the east asian region, Technical report, Network Center for EANET, 2011.

Adams, P. J. and Seinfeld, J. H.: Predicting global aerosol size distribution in general circulation models, J. Geophys. Res., 107, 4370, doi:10.1029/2001JD001010, 2002.

Adams, P. J., Seinfeld, J. H., and Koch, D.: Global concentrations of tropospheric sulfate, nitrate, and ammonium aerosol simulated in a general circulation model, J. Geophys. Res., 104, 13791–13824, doi:10.1029/1999JD900083, 1999.

Ames, R. and Malm, W.: Comparison of sulfate and nitrate particle mass concentrations measured by IMPROVE and the CDN, Atmos. Environ., 35, 905–916, doi:10.1016/S1352-2310(00)00369-1, 2001.

Appel, B., Tokiwa, Y., Kothny, E., Wu, R., and Povard, V.: Evaluation of procedures for measuring atmospheric nitric acid and ammonia, Atmos. Environ., 22, 1565–1573, 1988.

Atwater, M. A.: Thermal changes induced by urbanization and pollutants, Appl. Meteorol., 14, 1061–1071, 1975.

Baklanov, A.: Numerical Modelling in Mine Aerology, Apatity: USSR Academy of Science, 200 pp., 1988 (in Russian).

Barna, M. and Lamb, B.: Improving ozone modeling in regions of complex terrain using observational nudging in a prognostic meteorological model, Atmos. Environ., 34, 4889–4906, doi:10.1016/S1352-2310(00)00231-4, 2000.

Battye, W., Aneja, V. P., and Roelle, P. A.: Evaluation and improvement of ammonia emissions inventories, Atmos. Environ., 37, 3873–3883, doi:10.1016/S1352-2310(03)00343-1, 2003.

Bauer, S. E. and Koch, D.: Impact of heterogeneous sulfate formation at mineral dust surfaces on aerosol loads and radiative forcing in the Goddard Institute for Space Studies general circulation model, J. Geophys. Res., 110, D17202, doi:10.1029/2005JD005870, 2005.

Bauer, S. E., Koch, D., Unger, N., Metzger, S. M., Shindell, D. T., and Streets, D. G.: Nitrate aerosols today and in 2030: a global simulation including aerosols and tropospheric ozone, Atmos. Chem. Phys., 7, 5043–5059, doi:10.5194/acp-7-5043-2007, 2007.

Bond, T., Bhardwaj, E., Dong, R., Jogani, R., Jung, S., Roden, C., Streets, D., and Trautmann, N.: Historical emissions of black and organic carbon aerosol from energy-related combustion, 1850–2000, Global Biogeochem. Cy., 21, GB2018, doi:10.1029/2006GB002840, 2007.

Bouwman, A., Lee, D., Asman, W., Dentener, F., Van Der Hoek, K., and Olivier, J.: A global high-resolution emission inventory for ammonia, Global Biogeochem. Cy., 4, 561–587, 1997.

Broadgate, W., Liss, P., and Penkett, A.: Seasonal emission of isoprene and other reactive hydrocarbon gases from the ocean, Geophys. Res. Lett., 24, 2675–2678, 2000.

Clarisse, L., Clerbaux, C., Dentener, F., Hurtmans, D., and Coheur, P.-F.: Global ammonia distribution derived from infrared satellite observations, Nat. Geosci., 2, 479–483, doi:10.1038/ngeo551, 2009.

Conkright, M., O'Brien, T., Stephens, C., Locarnini, R., Garcia, H., Boyer, T., and Antonov, J.: World Ocean Atlas 2001, Vol. 6: Chlorophyll, NOOA Atlas NESDIS 52, US Government Printing Office, 46 pp., 2002.

de Meij, A., Krol, M., Dentener, F., Vignati, E., Cuvelier, C., and Thunis, P.: The sensitivity of aerosol in Europe to two different emission inventories and temporal distribution of emissions, Atmos. Chem. Phys., 6, 4287–4309, doi:10.5194/acp-6-4287-2006, 2006.

Dentener, F., Kinne, S., Bond, T., Boucher, O., Cofala, J., Generoso, S., Ginoux, P., Gong, S., Hoelzemann, J. J., Ito, A., Marelli, L., Penner, J. E., Putaud, J.-P., Textor, C., Schulz, M., van der Werf, G. R., and Wilson, J.: Emissions of primary aerosol and precursor gases in the years 2000 and 1750 prescribed data-sets for AeroCom, Atmos. Chem. Phys., 6, 4321–4344, doi:10.5194/acp-6-4321-2006, 2006.

Dimitroulopoulou, C. and ApSimon, H. M.: The influence of the photolysis rates on modelled ozone concentrations, Atmos. Environ., 33, 147–154, 1999.

Diner, D., Beckert, J., Reilly, T., Bruegge, C., Conel, J., Kahn, R., Martonchik, J., Ackerman, T., Davies, R., Gerstl, S., Gordon, H., Muller, J.-P., Myneni, R., Sellers, P., Pinty, B., and Verstraete, M.: Multi-angle Imaging SpectroRadiometer (MISR) instrument description and experiment overview, IEEE T. Geosci. Remote, 36, 3113–3136, doi:10.1109/36.700992, 1998.

Doering, U., Monni, S., Pagliari, V., Orlandini, L., van Aardenne, and SanMartin, F.: CIRCE report D8.1.1 – Emission inventory for the past period 1990–2005 on 0.1×0.1 grid, Tech. rep., Project FP6: 6.3, No. 036961, 2009a.

Doering, U., van Aardenne, J., Monni, S., Pagliari, V., Orlandini, L., and SanMartin, F.: CIRCE report D8.1.2 – Evaluation emission database 1990–2005, Tech. rep., Project FP6: 6.3, No. 036961, 2009b.

Doering, U., van Aardenne, J., Monni, S., Pagliari, V., Orlandini, L., and SanMartin, F.: CIRCE report D8.1.3 – Update of gridded emission inventories, addition of period 1990–2005 and the years 2010, 2015, 2050, Tech. rep., Project FP6: 6.3, No. 036961, 2009c.

Edgerton, E., Lavery, T., Hodges, M., and Bowser, J.: National Dry Deposition Network: Second Annual Progress Report (1988), Epa/600/3-90/020, Environmental Protection Agency, Research Triangle Park, NC, 1990.

Eyers, C. J., Addleton, D., Atkinson, K., Broomhead, M. J., Christou, R., Elliff, T., Falk, R., Gee, I., Lee, D., Marizy, C., Michot, S., Middel, J., Newton, P., Norman, P., Plohr, M., Raper, D., and Stanciou, N.: AERO2k, Global Aviation Emissions Inventories for 2002 and 2025, Tech. rep., QinetiQ Ltd, Farnborough, Hampshire QINETIQ/04/01113, 2004.

Feng, Y. and Penner, J.: Global modeling of nitrate and ammonium: interaction of aerosols and tropospheric chemistry, J. Geophys. Res., 112, D01304, doi:10.1029/2005JD006404, 2007.

Fountoukis, C. and Nenes, A.: ISORROPIA II: a computationally efficient thermodynamic equilibrium model for K^+–Ca^{2+}–Mg^{2+}–NH_4^+–Na^+–SO_4^{2-}–NO_3^-–Cl^-–H_2O aerosols, Atmos. Chem. Phys., 7, 4639–4659, doi:10.5194/acp-7-4639-2007, 2007.

Ganzeveld, L. N., van Aardenne, J. A., Butler, T. M., Lawrence, M. G., Metzger, S. M., Stier, P., Zimmermann, P., and Lelieveld, J.: Technical Note: Anthropogenic and natural offline emissions and the online EMissions and dry DEPosition submodel EMDEP of the Modular Earth Submodel system (MESSy), Atmos. Chem. Phys. Discuss., 6, 5457–5483, doi:10.5194/acpd-6-5457-2006, 2006.

Giglio, L., Randerson, J. T., van der Werf, G. R., Kasibhatla, P. S., Collatz, G. J., Morton, D. C., and DeFries, R. S.: Assessing variability and long-term trends in burned area by merging multiple satellite fire products, Biogeosciences, 7, 1171–1186, doi:10.5194/bg-7-1171-2010, 2010.

Goebes, M. D., Strader, R., and Davidson, C.: An ammonia emission inventory for fertilizer application in the United States, Atmos. Environ., 37, 2539–2550, doi:10.1016/S1352-2310(03)00129-8, 2003.

Guenther, A., Hewitt, C. N., Erickson, D., Fall, R., Geron, C., Graedel, T., Harley, P., Klinger, L., Lerdau, M., McKay, W. A., Pierce, T., Scholes, B., Steinbrecher, R., Tallamraju, R., Taylor, J., and Zimmerman, P.: A global model of natural volatile organic compound emissions, J. Geophys. Res., 100, 8873–8892, 1995.

Hale, G. and Querry, M.: Optical constants of water in the 200-nm to 200-µm wavelength region, Appl. Optics, 12, 555–563, 1973.

Hering, S. and Cass, G.: The magnitude of bias in the measurement of $PM_{2.5}$ arising from volatilization of particulate nitrate from Teflon filters, J. Air Waste Manage., 46, 725–733, 1999.

Hess, M., Koepke, P., and Schult, I.: Optical properties of aerosols and clouds: the software package OPAC, B. Am. Meteorol. Soc., 79, 831–844, 1998.

Hjellbrekke, A.-G. and Fjæraa, A.M.: Acidifying and eutrophying compounds and particulate matter, Technical report, Norwegian Meteorological Institute, Oslo, Norway, 2011.

Hofmann, C., Kerkweg, A., Wernli, H., and Jöckel, P.: The 1-way on-line coupled atmospheric chemistry model system MECO(n) – Part 3: Meteorological evaluation of the on-line coupled system, Geosci. Model Dev. Discuss., 4, 1533–1567, doi:10.5194/gmdd-4-1533-2011, 2011.

Hoor, P., Borken-Kleefeld, J., Caro, D., Dessens, O., Endresen, O., Gauss, M., Grewe, V., Hauglustaine, D., Isaksen, I. S. A., Jöckel, P., Lelieveld, J., Myhre, G., Meijer, E., Olivie, D., Prather, M., Schnadt Poberaj, C., Shine, K. P., Staehelin, J., Tang, Q., van Aardenne, J., van Velthoven, P., and Sausen, R.: The impact of traffic emissions on atmospheric ozone and OH: results from QUANTIFY, Atmos. Chem. Phys., 9, 3113–3136, doi:10.5194/acp-9-3113-2009, 2009.

Huntingford, C., Hemming, D., Gash, J., Gedney, N., and Nuttall, P.: Impact of climate change on health: what is required of climate modellers?, T. Roy. Soc. Trop. Med. H., 101, 97–103, doi:10.1016/j.trstmh.2006.11.001, 2007.

Isaksen, I., Granier, C., Myhre, G., Berntsen, T., Dalsøren, S., Gauss, M., Klimont, Z., Benestad, R., Bousquet, P., Collins, W., Cox, T., Eyring, V., Fowler, D., Fuzzi, S., Jöckel, P., Laj, P., Lohmann, U., Maione, M., Monks, P., Prevot, A. S. H., Raes, F., Richter, A., Rognerud, B., Schulz, M., Shindell, D., Stevenson, D. S., Storelvmo, T., Wang, W.-C., van Weele, M., Wild, M., and Wuebbles, D.: Atmospheric composition change: climate-chemistry interactions, Atmos. Environ., 43, 5138–5192, 2009.

Jacobson, M. Z.: Development and application of a new air pollution modeling system, Part II: Aerosol module structure and design, Atmos. Environ., 31, 131–144, 1997a.

Jacobson, M. Z.: Development and application of a new air pollution modeling system, Part III: Aerosol-phase simulation, Atmos. Environ., 31A, 587–608, 1997b.

Jacobson, M. Z.: A physically-based treatment of elemental carbon optics: Implication for globak direct forcing of aerosol, Geophys. Res. Lett., 27, 217–220, 2000.

Jacobson, M. Z.: Global direct radiative forcing due to multicomponent anthropogenic and natural aerosols, J. Geophys. Res., 106, 1551–1568, 2001a.

Jacobson, M. Z.: Strong radiative heating due to the mixing state of black carbon in atmospheric aerosols, Nature, 409, 695–697, 2001b.

Jacobson, M. Z.: GATOR-GCMM. 2, a study of daytime and nighttime ozone layers aloft, ozone in national parks, and weather during the SARMAP field campaign J. Geophys. Res., 106, 5403–5420, 2001c.

Jacobson, M. Z., Kaufmann, Y. J., and Rudich, Y.: Examining feedbacks of aerosols to urban climate with a model that treats 3-d clouds with aerosol inclusions, J. Geophys. Res, 112, D24205, doi:10.1029/2007JD008922, 2007.

Jacobson, M. Z.: Short-term effects of controlling fossil-fuel soot, biofuel soot and gases, and methane on climate, arctic ice, and air pollution health, J. Geophys. Res, 115, D14209, doi:10.1029/2009JD013795, 2010.

Jeuken, A., Siegmund, P., Heijboer, L., Feichter, J., and Bengtsson, L.: On the potential assimilating meteorological analyses in a global model for the purpose of model validation, J. Geophys. Res., 101, 16939–16950, 1996.

Jöckel, P., Sander, R., Kerkweg, A., Tost, H., and Lelieveld, J.: Technical Note: The Modular Earth Submodel System (MESSy) – a new approach towards Earth System Modeling, Atmos. Chem. Phys., 5, 433–444, doi:10.5194/acp-5-433-2005, 2005.

Jöckel, P., Tost, H., Pozzer, A., Brühl, C., Buchholz, J., Ganzeveld, L., Hoor, P., Kerkweg, A., Lawrence, M. G., Sander, R., Steil, B., Stiller, G., Tanarhte, M., Taraborrelli, D., van Aardenne, J., and Lelieveld, J.: The atmospheric chemistry general circulation model ECHAM5/MESSy1: consistent simulation of ozone from the surface to the mesosphere, Atmos. Chem. Phys., 6, 5067–5104, doi:10.5194/acp-6-5067-2006, 2006.

Kahn, R. A., Gaitley, B. J., Martonchik, J. V., Diner, D. J., Crean, K. A., and Holben, B.: Multiangle Imaging Spectroradiometer (MISR) global aerosol optical depth validation based on 2 years of coincident Aerosol Robotic Network (AERONET) observations, J. Geophys. Res., 110, 0148–0227, doi:10.1029/2004JD004706, 2005.

Kahn, R. A., Gaitley, B. J., Garay, M., Diner, D. J., Eck, T., A., S., and Holben, B.: Multiangle Imaging Spectroradiometer (MISR) global aerosol optical depth validation based on 2 years of coincident Aerosol Robotic Network (AERONET) observations, J. Geophys. Res., 115, 0148–0227, doi:10.1029/2010JD014601, 2010.

Kaufman, Y. J., Tanré, D., Remer, L. A., Vermote, E. F., Chu, A., and Holben, B. N.: Multiangle Imaging Spectroradiometer (MISR) global aerosol optical depth validation based on 2 years of coincident Aerosol Robotic Network (AERONET) observations, J. Geophys. Res., 102, 17051–17068, doi:10.1029/96JD03988, 1997.

Kerkweg, A. and Jöckel, P.: The 1-way on-line coupled atmospheric chemistry model system MECO(n) – Part 2: On-line coupling, Geosci. Model Dev. Discuss., 4, 1359-1402, doi:10.5194/gmdd-

4-1359-2011, 2011.

Kerkweg, A., Buchholz, J., Ganzeveld, L., Pozzer, A., Tost, H., and Jöckel, P.: Technical Note: An implementation of the dry removal processes DRY DEPosition and SEDImentation in the Modular Earth Submodel System (MESSy), Atmos. Chem. Phys., 6, 4617–4632, doi:10.5194/acp-6-4617-2006, 2006a.

Kerkweg, A., Sander, R., Tost, H., and Jöckel, P.: Technical note: Implementation of prescribed (OFFLEM), calculated (ONLEM), and pseudo-emissions (TNUDGE) of chemical species in the Modular Earth Submodel System (MESSy), Atmos. Chem. Phys., 6, 3603–3609, doi:10.5194/acp-6-3603-2006, 2006b.

Kettle, A., Andreae, M., Amouroux, D., Andreae, T., Bates, T., Berresheim, H., Bingemer, H., Boniforti, R., Curran, M., DeTullio, G., Helas, G., Jones, G., Keller, M., Kiene, R., Leck, C., Levasseur, M., Maspero, M., Matraii, P., McTaggart, A., Mihalopoulos, N., Nguyen, B., Novo, A., Putaud, J. P., P., Rapsomanikis, S., Roberts, G., Schebeske, G., Sharma, S., Simo, R., Staubes, R., Turner, S., and Uher, G.: A global database of sea surface dimethylsulfide (DMS) measurements and a simple model to predict sea surface DMS as a function of latitude, longitude and month, Global Biogeochem. Cy., 13, 399–444, 1999.

Kiehl, J. and Briegleb, B.: The relative roles of sulfate aerosols and greenhouse gases in climate forcing, Science, 260, 311–314, doi:10.1126/science.260.5106.311 1993.

Klimont, Z., Streets, D., Gupta, S., Cofala, J., Lixin, F., and Ichikawa, Y.: Anthropogenic emissions of non-methane volatile organic compounds in China, Atmos. Environ., 36, 1309–1322, 2002.

Lauer, A., Eyring, V., Hendricks, J., Jöckel, P., and Lohmann, U.: Global model simulations of the impact of ocean-going ships on aerosols, clouds, and the radiation budget, Atmos. Chem. Phys., 7, 5061–5079, doi:10.5194/acp-7-5061-2007, 2007.

Lawrence, M. G., Butler, T. M., Steinkamp, J., Gurjar, B. R., and Lelieveld, J.: Regional pollution potentials of megacities and other major population centers, Atmos. Chem. Phys., 7, 3969–3987, doi:10.5194/acp-7-3969-2007, 2007.

Lelieveld, J., Brühl, C., Jöckel, P., Steil, B., Crutzen, P. J., Fischer, H., Giorgetta, M. A., Hoor, P., Lawrence, M. G., Sausen, R., and Tost, H.: Stratospheric dryness: model simulations and satellite observations, Atmos. Chem. Phys., 7, 1313–1332, doi:10.5194/acp-7-1313-2007, 2007.

Levy, R. C., Remer, L. A., Kleidman, R. G., Mattoo, S., Ichoku, C., Kahn, R., and Eck, T. F.: Global evaluation of the Collection 5 MODIS dark-target aerosol products over land, Atmos. Chem. Phys., 10, 10399–10420, doi:10.5194/acp-10-10399-2010, 2010.

Lin, J.-T., Youn, D., Liang, X.-Z., and Wuebbles, D. J.: Global model simulation of summertime U.S. ozone diurnal cycle and its sensitivity to pbl mixing, spatial resolution, and emissions, Atmos. Environ., 42, 8470–8483, doi:10.1016/j.atmosenv.2008.08.012, 2008.

Liu, C., Beirle, S., Butler, T., Liu, J., Hoor, P., Jöckel, P., Pozzer, A., Frankenberg, C., Lawrence, M. G., Lelieveld, J., Platt, U., and Wagner, T.: Application of SCIAMACHY and MOPITT CO total column measurements to evaluate model results over biomass burning regions and Eastern China, Atmos. Chem. Phys., 11, 6083–6114, doi:10.5194/acp-11-6083-2011, 2011.

Ma, J., Chen, A., Wang, W., Yan, P., Liu, H., Yang, S., Hu, Z., and Lelieveld, J.: Strong air pollution causes widespread haze-clouds over China, J. Geophys. Res., 115, D18204, doi:10.1029/2009JD013065, 2010.

Manders, A. M. M., Schaap, M., Querol, X., Albert, M. F. M. A., Vercauteren, J., Kuhlbusch, T. A. J., and Hoogerbrugge, R.: Sea salt concentrations across the European continent, Atmos. Environ., 44, 2434–2442, doi:10.1016/j.atmosenv.2010.03.028, 2010.

Mann, G. W., Carslaw, K. S., Spracklen, D. V., Ridley, D. A., Manktelow, P. T., Chipperfield, M. P., Pickering, S. J., and Johnson, C. E.: Description and evaluation of GLOMAP-mode: a modal global aerosol microphysics model for the UKCA composition-climate model, Geosci. Model Dev., 3, 519–551, doi:10.5194/gmd-3-519-2010, 2010.

Maring, H., Savioe, D. L., Izaguirre, M. A., Custals, L., and Reid, J. S.: Vertical distributions of dust and sea-salt aerosols over Puerto Rico during PRIDE measured from a light aircraft, J. Geophys. Res., D19, 8587–8598, doi:10.1029/2002JD002544, 2003.

Mayer, B. and Kylling, A.: Technical note: The libRadtran software package for radiative transfer calculations – description and examples of use, Atmos. Chem. Phys., 5, 1855–1877, doi:10.5194/acp-5-1855-2005, 2005.

McInnes, L. M., Covert, D. S., Quinn, P. K., and Germani, M. S.: Measurements of chloride depletion and sulfur enrichment in individual sea-salt particles collected from the remote marine boundary layer, J. Geophys. Res., 99, 8257–8268, doi:10.1029/93JD03453, 1994.

Millero, F. J.: Physicochemical controls on seawater, Treatise Geochem., 6, 1–21, 2003.

Myhre, G., Grini, A., and Metzger, S.: Modelling of nitrate and ammonium-containing aerosols in presence of sea salt, Atmos. Chem. Phys., 6, 4809–4821, doi:10.5194/acp-6-4809-2006, 2006.

Nenes, A., Pandis, S. N., and Pilinis, C.: ISORROPIA: a new thermodynamic equilibrium model for multiphase multicomponent inorganic aerosols, Aquat. Geochem., 1, 123–152, doi:10.1023/A:1009604003981, 1998a.

Nenes, A., Pandis, S. N., and Pilinis, C.: Continued development and testing of a new thermodynamic aerosol module for urban and regional air quality models, Atmos. Environ., 33, 1553–1560, 1998b.

Ohara, T., Akimoto, H., Kurokawa, J., Horii, N., Yamaji, K., Yan, X., and Hayasaka, T.: An Asian emission inventory of anthropogenic emission sources for the period 1980–2020, Atmos. Chem. Phys., 7, 4419–4444, doi:10.5194/acp-7-4419-2007, 2007.

Olivier, J. G. J., Bouwman, A. F., van der Maas, C. W. M., Berdowski, J. J. M., Veldt, C., Bloos, J. P. J., Visschedijk, A. J. J., Zandveld, P. Y. J., and Haverlag, J. L.: Description of EDGAR Version 2.0: a set of global inventories of greenhouse gases and ozone-depleting substances for all anthrophogenic and most natural sources on a per country $1^\circ \times 1^\circ$ grid, RIVM Rep. 771060002, Rijksinstituut, Bilthoven, Netherlands, 1996.

Olivier, J. G. J., Bloos, J. P. J., Berdowski, J. J. M., Visschedijk, A. J. H., and Bouwman, A. F.: A 1990 global emission inventory of anthropogenic sources of carbon monoxide on $1^\circ \times 1^\circ$ developed in the framework of EDGAR/GEIA, Chemosphere, 1, 1–17, 1999.

Olson, J.: World Ecosystems (WE1.4): Digital Raster Data on a 10 min Geographic 1080×2160 Grid Square, Global Ecosystem Database, ISBN 92-63-02182-1, NOAA, publisher, National

Geophysical Data Center, Boulder, Colorado, 1992.

Park, R. J., Pickering, K. E., Allen, D. J., Stenchikov, G. L., and Fox-Rabinovitz, M. S.: Global simulation of tropospheric ozone using the university of maryland chemical transport model (UMD-CTM): 1. model description and evaluation, J. Geophys. Res., 109, D0930 doi:10.1029/2003JD004266, 2004a.

Park, R. J., Pickering, K. E., Allen, D. J., Stenchikov, G. L., and Fox-Rabinovitz, M. S.: Global simulation of tropospheric ozone using the university of maryland chemical transport model (UMD-CTM): 2. regional transport and chemistry over the central united states using a stretched grid. J. Geophys. Res., 109, D09303 doi:10.1029/2003JD004269, 2004b.

Pinder, R. W., Strader, R., Davidson, C. I., and Adams, P. J.: A temporally and spatially resolved ammonia emission inventory for dairy cows in the United States, Atmos. Environ., 38, 3747–3756, doi:10.1016/j.atmosenv.2004.04.008, 2004.

Pozzer, A., Jöckel, P., Sander, R., Williams, J., Ganzeveld, L., and Lelieveld, J.: Technical Note: The MESSy-submodel AIRSEA calculating the air-sea exchange of chemical species, Atmos. Chem. Phys., 6, 5435–5444, doi:10.5194/acp-6-5435-2006, 2006.

Pozzer, A., Jöckel, P., Tost, H., Sander, R., Ganzeveld, L., Kerkweg, A., and Lelieveld, J.: Simulating organic species with the global atmospheric chemistry general circulation model ECHAM5/MESSy1: a comparison of model results with observations, Atmos. Chem. Phys., 7, 2527–2550, doi:10.5194/acp-7-2527-2007, 2007.

Pozzer, A., Jöckel, P., and Van Aardenne, J.: The influence of the vertical distribution of emissions on tropospheric chemistry, Atmos. Chem. Phys., 9, 9417–9432, doi:10.5194/acp-9-9417-2009, 2009.

Price, C. and Rind, D.: A simple lightning parameterization for calculating global lightning distributions, J. Geophys. Res., 97, 9919–9933, 1992.

Pringle, K. J., Tost, H., Message, S., Steil, B., Giannadaki, D., Nenes, A., Fountoukis, C., Stier, P., Vignati, E., and Lelieveld, J.: Description and evaluation of GMXe: a new aerosol submodel for global simulations (v1), Geosci. Model Dev., 3, 391–412, doi:10.5194/gmd-3-391-2010, 2010a.

Pringle, K. J., Tost, H., Pozzer, A., Pöschl, U., and Lelieveld, J.: Global distribution of the effective aerosol hygroscopicity parameter for CCN activation, Atmos. Chem. Phys., 10, 5241–5255, doi:10.5194/acp-10-5241-2010, 2010b.

Pye, H., Liao, H., Wu, S., Mickley, L., Jacob, D., Henze, D., and Seinfeld, J.: Effect of changes in climate and emissions on future sulfate-nitrate-ammonium aerosol levels in the United States, J. Geophys. Res., 114, 1–18, 2009.

Ramanathan, V., Crutzen, P., Kiehl, J., and Rosenfeld, D.: Aerosols, climate, and the hydrological cycle, Science, 294, 2119–2124, doi:10.1126/science.1064034, 2001.

Remer, L., Kleidman, R., Levy, R., Kaufman, Y., Tanré, D., Mattoo, S., Martins, J., Ichoku, C., Koren, I., Yu, H., and Holben, B. H.: Global aerosol climatology from the MODIS satellite sensors, J. Geophys. Res., 113, D14S07, doi:10.1029/2007JD009661, 2008.

Rodriguez, M. and Dabdub, D.: IMAGES-SCAPE2: a modeling study of size-and chemically resolved aerosol thermodynamics in a global chemical transport model, J. Geophys. Res., 109, D02203, doi:10.1029/2003JD003639, 2004.

Roeckner, E., Brokopf, R., Esch, M., Giorgetta, M., Hagemann, S., Kornblueh, L., Manzini, E., Schlese, U., and Schulzweida, U.: Sensitivity of simulated climate to horizontal and vertical resolution in the ECHAM5 atmosphere model, J. Climate, 19, 3771–3791, 2006.

Sander, R., Kerkweg, A., Jöckel, P., and Lelieveld, J.: Technical note: The new comprehensive atmospheric chemistry module MECCA, Atmos. Chem. Phys., 5, 445–450, doi:10.5194/acp-5-445-2005, 2005.

Schaap, M.: On the importance of aerosol nitrate in Europe, Data analysis and modelling, Ph.D. thesis, University of Utrecht, available at: http://www.library.uu.nl/digiarchief/dip/diss/2003-1209-110044/inhoud.htm, 2003.

Schaap, M., van Loon, M., ten Brink, H. M., Dentener, F. J., and Builtjes, P. J. H.: Secondary inorganic aerosol simulations for Europe with special attention to nitrate, Atmos. Chem. Phys., 4, 857–874, doi:10.5194/acp-4-857-2004, 2004.

Shettle, E.: Models for the Aerosols of the Lower Atmosphere and the Effects of Humidity Variations on their Optical Properties, Tech. Rep. ADA085951, Air Force Geophysics Lab, Hanscom AFB MA, 1979.

Simpson, D., Fagerli, H., Jonson, J., Tsyro, S., Wind, P., and Tuovinen, J.-P.: Transboundary acidification and eutrophication and ground level ozone in Europe: Unified EMEP Model Description., Tech. rep., Norwegian Meteorological Institute, Oslo, Norway, 2003.

Stier, P., Feichter, J., Kinne, S., Kloster, S., Vignati, E., Wilson, J., Ganzeveld, L., Tegen, I., Werner, M., Balkanski, Y., Schulz, M., Boucher, O., Minikin, A., and Petzold, A.: The aerosol-climate model ECHAM5-HAM, Atmos. Chem. Phys., 5, 1125–1156, doi:10.5194/acp-5-1125-2005, 2005.

Streets, D. and Waldhoff, S.: Present and future emissions of air pollutants in China: SO_2, NO_x, and CO, Atmos. Environ., 34, 363–374, 2000.

Streets, D., Bond, T. C., Carmichael, G. R., Fernandes, S. D., Fu, Q., He, D., Klimont, Z., Nelson, S. M., Tsai, N. Y., Wang, M. Q., Woo, J. H., and Yarber, K. F.: An inventory of gaseous and primary aerosol emission in Asia in the year 2000, J. Geophys. Res., 108, 8809, doi:10.1029/2002JD003093, 2003.

Sutherland, R. and Khanna, R.: Optical properties of organic-based aerosols produced by burning vegetation, Aerosol Sci. Tech., 14, 331–342, 1991.

Tanré, D., Kaufman, Y. J., Herman, M., and Mattoo, S.: Multiangle Imaging Spectroradiometer (MISR) global aerosol optical depth validation based on 2 years of coincident Aerosol Robotic Network (AERONET) observations, J. Geophys. Res., 102, 16971–16988, doi:10.1029/96JD03437, 1997.

Taylor, K.: Summarizing multiple aspects of model performance in a single diagram, J. Geophys. Res., 106, 7183–7192, 2001.

Taylor, K. E. and Penner, J. E.: Response of the climate system to the atmospehric aerosols and greenhouse gases, Nature, 369, 734–737, doi:10/1038/369734a0, 1994.

Textor, C., Schulz, M., Guibert, S., Kinne, S., Balkanski, Y., Bauer, S., Berntsen, T., Berglen, T., Boucher, O., Chin, M., Dentener, F., Diehl, T., Easter, R., Feichter, H., Fillmore, D., Ghan, S., Ginoux, P., Gong, S., Grini, A., Hendricks, J., Horowitz, L., Huang, P., Isaksen, I., Iversen, I., Kloster, S., Koch, D., Kirkevåg, A., Kristjansson, J. E., Krol, M., Lauer, A., Lamarque, J. F., Liu, X., Montanaro, V., Myhre, G., Penner, J., Pitari, G., Reddy, S., Seland, Ø., Stier, P., Takemura, T., and Tie, X.: Analysis and quantification of the diversities of aerosol life cycles within AeroCom, Atmos. Chem. Phys., 6, 1777–1813, doi:10.5194/acp-6-1777-2006, 2006.

Tost, H., Jöckel, P., Kerkweg, A., Sander, R., and Lelieveld, J.: Technical note: A new comprehensive SCAVenging submodel for global atmospheric chemistry modelling, Atmos. Chem. Phys., 6, 565–574, doi:10.5194/acp-6-565-2006, 2006a.

Tost, H., Jöckel, P., and Lelieveld, J.: Influence of different convection parameterisations in a GCM, Atmos. Chem. Phys., 6, 5475–5493, doi:10.5194/acp-6-5475-2006, 2006b.

Tost, H., Jöckel, P., Kerkweg, A., Pozzer, A., Sander, R., and Lelieveld, J.: Global cloud and precipitation chemistry and wet deposition: tropospheric model simulations with ECHAM5/MESSy1, Atmos. Chem. Phys., 7, 2733–2757, doi:10.5194/acp-7-2733-2007, 2007a.

Tost, H., Jöckel, P., and Lelieveld, J.: Lightning and convection parameterisations – uncertainties in global modelling, Atmos. Chem. Phys., 7, 4553–4568, doi:10.5194/acp-7-4553-2007, 2007b.

UNECE/UNFCCC: National Communication United Nations Framework Convention on Climate Change, http://unfccc.int, last access: 1 August 2011, 2008.

Vestreng, V. and Klein, H.: Emission data reported to UNECE/EMEP: quality assurance and trend analysis and presentation of WebDab, MSC-W Status Rep. 2002, Norw. Meteorol. Inst., Oslo, Norway, 2002.

Vestreng, V., Myhre, G., Fagerli, H., Reis, S., and Tarrasón, L.: Twenty-five years of continuous sulphur dioxide emission reduction in Europe, Atmos. Chem. Phys., 7, 3663–3681, doi:10.5194/acp-7-3663-2007, 2007.

Vestreng, V., Ntziachristos, L., Semb, A., Reis, S., Isaksen, I. S. A., and Tarrasón, L.: Evolution of NO_x emissions in Europe with focus on road transport control measures, Atmos. Chem. Phys., 9, 1503–1520, doi:10.5194/acp-9-1503-2009, 2009.

Vignati, E., Wilson, J., and Stier, P.: M7: an efficient size-resolved aerosol microphysics module for large-scale aerosol transport models, J. Geophys. Res., 109, D22202, doi:10.1029/2003JD004485, 2004.

van Aardenne, J., Dentener, F., Olivier, J., Peters, J., and Ganzeveld, L.: The EDGAR 3.2 Fast Track 2000 Dataset (32FT2000), http://www.mnp.nl/edgar/model/v32ft2000edgar/docv32ft2000/, 2005.

van der Werf, G. R., Randerson, J. T., Giglio, L., Collatz, G. J., Mu, M., Kasibhatla, P. S., Morton, D. C., DeFries, R. S., Jin, Y., and van Leeuwen, T. T.: Global fire emissions and the contribution of deforestation, savanna, forest, agricultural, and peat fires (1997–2009), Atmos. Chem. Phys., 10, 11707–11735, doi:10.5194/acp-10-11707-2010, 2010.

von Kuhlmann, R., Lawrence, M. G., Crutzen, P. J., and Rasch, P. J.: A Model for Studies of Tropospheric Ozone and Non-Methane Hydrocarbons: Model Evaluation of Ozone related species, J. Geophys. Res., 108, 4729, doi:10.1029/2002JD003348, 2003.

Wanninkhof, R.: Relationship between wind speed and gas exchange over the ocean, J. Geophys. Res., 97, 7373–7382, 1992.

Warneke, C., McKeen, S. A., De Gouw, J. A., Goldan, P. D., Kuster, W. C., Holloway, J. S., Williams, E. J., Lerner, B. M., Parrish, D. D., Trainer, M. Fehsenfeld, F. C., Kato, S., Atlas, E. L., Baker, A., and Blake, D. R.: Determination of urban volatile organic compound emission ratios and comparison with an emissions database, J. Geophys. Res, 112, D10S47, doi:10.1029/2006JD007930, 2007

White, W. H.: Chemical markers for sea salt in IMPROVE aerosol data, Atmos. Environ., 42, 261–274, doi:10.1016/j.atmosenv.2007.09.040, 2008.

Wild, O. and Prather, M. J.: Global tropospheric ozone modeling: Quantifying errors due to grid resolution, J. Geophys. Res., 111, D11305, doi:10.1029/2005JD006605, 2006.

Yienger, J. J. and Levy, H.: Empirical model of global soil-biogenic NO_x emissions, J. Geophys. Res., 100, 11447–11464, 1995.

Zhang, Q., Streets, D. G., Carmichael, G. R., He, K. B., Huo, H., Kannari, A., Klimont, Z., Park, I. S., Reddy, S., Fu, J. S., Chen, D., Duan, L., Lei, Y., Wang, L. T., and Yao, Z. L.: Asian emissions in 2006 for the NASA INTEX-B mission, Atmos. Chem. Phys., 9, 5131–5153, doi:10.5194/acp-9-5131-2009, 2009.

Zhang, Y.: Online-coupled meteorology and chemistry models: history, current status, and outlook, Atmos. Chem. Phys., 8, 2895–2932 doi:10.5194/acp-8-2895-2008, 2008.